Grujic Djordje (Orcid ID: 0000-0002-5833-8843)
Ashley Kyle, Thomas (Orcid ID: 0000-0002-8588-9712)
Coble Matthew, A (Orcid ID: 0000-0002-7536-0559)
Coutand Isabelle (Orcid ID: 0000-0002-5039-658X)
Kellett Dawn, A. (Orcid ID: 0000-0002-4558-4703)
Larson Kyle (Orcid ID: 0000-0002-1850-1896)
Whipp David, Michael (Orcid ID: 0000-0002-3820-6886)

# Deformational temperatures across the Lesser Himalayan Sequence in eastern Bhutan and their implications for the deformation history of the Main Central Thrust

**Djordje Grujic[1], Kyle T. Ashley[2], Matthew A. Coble[3], Isabelle Coutand[1], Dawn A. Kellett[4], Kyle P. Larson[5], David M. Whipp Jr.[6], Min Gao[1], and Nicholas Whynot[1]**

[1]Department of Earth Sciences, Dalhousie University, Halifax, NS, B3H 4R2, Canada.

[2]Department of Geological Sciences, Jackson School of Geosciences, University of Texas at Austin, Austin, TX 78712, USA.

[3]Department of Geological Science, Stanford University, CA 94305, USA.

[4]Geological Survey of Canada, 1 Challenger Dr., Dartmouth, NS, B2Y 4A2, Canada.

[5]Earth, Environmental and Geographic Sciences, University of British Columbia Okanagan, Kelowna, BC, Canada.

[6]Institute of Seismology, Department of Geosciences and Geography, University of Helsinki, Helsinki, Finland.

Corresponding author: Djordje Grujic (dgrujic@dal.ca)

**Key Points:**

- Crustal-scale shear zones produce inverted temperature fields with transient gradients.
- Each thermochronologic and thermobarometric method registers a different stage of such a temperature field.
- Numerical modeling of multiple thermochronological data sets permits more detailed and accurate reconstruction of the thermal history of crustal-scale shear zones.

This article has been accepted for publication and undergone full peer review but has not been through the copyediting, typesetting, pagination and proofreading process which may lead to differences between this version and the Version of Record. Please cite this article as doi: 10.1029/2019TC005914

**Abstract**

We postulate that the inverted metamorphic sequence in the Lesser Himalayan Sequence (LHS) of the Himalayan orogen is a finite product of its deformation and temperature history. To explain the formation of this inverted metamorphic sequence across the LHS with a focus on the Main Central Thrust (MCT) in eastern Bhutan, we determined the metamorphic peak temperatures by Raman spectroscopy of carbonaceous material (RSCM) and established the deformation temperatures by Ti-in-quartz thermobarometry and quartz *c*-axis textures. These data were combined with thermochronology, including new and published $^{40}Ar/^{39}Ar$ ages of muscovite and published apatite fission-track and apatite and zircon (U-Th)/He ages. To obtain accurate metamorphic, deformation and closure temperatures of thermochronological systems, pressures and cooling rates for the period of interest were derived by inverse modeling of multiple thermochronological datasets, and temperatures were determined by iterative calculations.

The RSCM results indicate two temperature sequences separated by a thrust. In the external sequence, peak temperatures are constant across the structural strike, consistent with the observed hinterland-dipping duplex system. In the internal temperature sequence associated with the MCT shear zone, each geothermometer yields an apparent inverted temperature gradient although with different temperature ranges, and all temperatures appear to be retrograde. These observations are consistent with the quartz microfabrics. Further, all thermochronometers indicate upward younging across the MCT.

We interpret our data as a composite peak and deformation temperature sequence that formed successively and reflects the broadening and narrowing of the MCT shear zone in which the ductile deformation lasted until ~11 Ma.

## 1 Introduction

Along its entire length, the Himalayan orogen exhibits an inverted metamorphic sequence up to several tens of kilometers wide in map view. The apparent peak metamorphic temperatures range across the strike of the Himalaya and structurally upward from lower greenschist-facies conditions with temperatures of ~350 °C to upper amphibolite facies at ~750 °C and local granulite-facies conditions (Beyssac et al., 2004; Caddick et al., 2007; Gaidies et al., 2015; Goscombe et al., 2018; Groppo et al., 2009; Kohn, 2014; Kohn et al., 2001; Mottram et al., 2014; Vannay et al., 1999; Warren et al., 2011; Waters, 2019; Yakymchuk & Godin, 2012). The steepest peak-temperature gradient is observed in the field and predicted in geodynamic models across the Main Central Thrust (MCT; Jamieson et al., 2004). The MCT is a crustal-scale, south-vergent, thrust sense, ductile shear zone characterized by a mylonite belt up to several kilometers wide (Searle et al., 2008, Starnes et al., 2020), which was active for ~10 million years. Geodynamic and thermokinematic models demonstrate that parallel to the displacement direction and perpendicular to the crustal-scale thrust, the strain and temperature are implicitly heterogeneous and that strain rates and temperature gradients are non-steady (e.g., Beaumont et al., 2004; Bollinger et al., 2004; Coutand et al., 2014; Jaquet and Schmalholz, 2018; this work). Flow stress estimates from natural mylonites based on various piezometric methods (e.g., Behr and Platt, 2014) indicate that the ductile middle crust below the brittle-ductile transition is the load-bearing element of the crust. Such studies, however, do not consider spatiotemporal changes in stresses or the effect of an inverted temperature gradient in a convergent setting in particular.

Our understanding of the tectonic evolution of the Himalaya has been dominated by studies of high-grade metamorphic rocks from the Greater Himalayan Sequence (GHS, also called the Higher Himalayan Crystalline) because rocks suitable for studies of pressure-temperature-time-deformation histories are present (Goscombe et al., 2018; Martin 2017;

Waters 2019). Given the inverted metamorphic sequence, this approach neglects critical information, as the majority of the inverted metamorphic field lies structurally beneath the GHS within the lower-grade Lesser Himalayan Sequence (LHS).

Considering that the LHS consists of a frontal duplex and the MCT zone separated by a thrust, the question arises of whether the entire LHS represents one continuous metamorphic sequence or rather several imbricated metamorphic domains. The relative contributions of basal accretion, post-metamorphic shearing of isotherms and synkinematic inversion of isotherms also remain principal questions related to the general formation of the inverted metamorphic field gradient. To address these questions and to quantify the peak-temperature gradient, we applied three geothermometric methods on a suite of samples located between the Main Boundary Thrust (MBT) and the Main Central Thrust (MCT) along a transect in eastern Bhutan. This is the best-exposed and best-studied segment of the LHS in Bhutan (Grujic et al., 1996, Daniel et. al., 2003; Chambers et al., 2011, Coutand et al., 2014, Hirschmiller et al., 2014; Gilmore et al., 2018; Long et al., 2011 a, d; 2012; McQuarrie et al., 2008, 2019, Singer et al., 2017), possibly in the Himalaya, and therefore provides the necessary foundation for this type of study. In this work, we focus on investigating the temperature history of LHS rocks affected by shearing along the MCT. However, we place our observations in the context of the complete section of the Himalayan orogen.

The Raman spectroscopy on carbonaceous material (RSCM) geothermometer, which does not depend on metamorphic index minerals (garnet, biotite, or chlorite) conspicuously lacking in most of the LHS, has been used to extract geothermometric data from the LHS (e.g., Beyssac et al., 2004; Célérier et al., 2009, Long et al., 2016). In this paper, we present RSCM metamorphic and quartz deformation temperature data (Ti-in-quartz and opening angles of quartz *c*-axis texture). To ascertain the ages of these temperatures, we used muscovite $^{40}Ar/^{39}Ar$ thermochronology. However, we did not measure the absolute age at

which measured temperatures were attained but set measured temperature data in relation to the $^{40}Ar/^{39}Ar$ ages and their individual closure temperatures. The closure temperature of the muscovite $^{40}Ar/^{39}Ar$ system depends on the cooling rate, which is traditionally simply assumed. Furthermore, the Ti concentration in quartz and diffusion of $^{40}Ar$ in muscovite are moderately pressure dependent. In shear zones with downdip displacement, the cooling rate is non-steady, and both the cooling rate and pressure at a specified temperature or time are difficult to constrain accurately because the strongly deformed temperature field and displacement along a ramp-flat surface decouple the exhumation and cooling. Combining new and published thermochronological results, we calculated for each sample the pressure and cooling rate at the period of interest by three-dimensional thermal-kinematic modeling and determined the deformation and closure temperatures by iterative calculations. Thus, the obtained time-temperature paths lead us to propose a qualitative model for the evolution of the deformation temperature field within the MCT zone.

## 2 Geological setting

### *2.1 Lithotectonic units*

The structure investigated in this study, the MCT (Martin, 2017, Searle et al., 2008; Starnes et al., 2020), separates two principal Himalayan lithotectonic units: the overlying GHS and the underlying LHS (Figure 1). The GHS consists of amphibolite- to granulite-facies para- and orthogneisses and Miocene migmatites and leucogranites (Corrie et al., 2012; Daniel et al., 2003; Davidson et al., 1997; Gansser, 1983; Regis et al., 2014; Swapp & Hollister, 1991; Warren et al., 2011). Between the GHS and the LHS, exposed along the entire Bhutan Himalaya, lies a thin lithotectonic unit called the Jaishidanda Formation (Dasgupta, 1995; Long et al., 2011d), which consists of biotite-muscovite- and locally garnet-bearing schist interbedded with biotite-rich quartzite and orthogneiss. This formation has

been interpreted as part of the underlying Daling-Shumar Group (Daniel et al., 2003), as a lithological unit in stratigraphic contact with the underlying Daling-Shumar Group (Long et al., 2011d, and references therein), or as a thin thrust sheet beneath the MCT in thrust contact over the Daling-Shumar Group (Bhargava, 1995). Because of the significant differences in metamorphic grade and inferred metamorphic path with respect to both underlying and overlying rocks (Chakungal, 2006), the Jaishidanda Formation is here considered a separate lithotectonic unit beneath the GHS but within the MCT shear zone (section 2.2).

In eastern Bhutan, the LHS is deformed into a southward-younging series of dominantly clastic marine and continental sediments of middle to late Paleozoic age (Long et al., 2011d; McQuarrie et al., 2008, and references therein) divided into four lithostratigraphic units (Figure 1). From north to south and structurally highest to lowest, these units are the Daling-Shumar Group, Baxa Group, Diuri Formation and Gondwana sequence (Bhargava, 1995; Gansser, 1983; Long et al., 2011d; McQuarrie et al., 2008). Although the highest structural units are stratigraphically the oldest and define an apparently inverted stratigraphic sequence, based on sedimentary structures, the individual lithostratigraphic units and beds are right side up, occasionally with preserved stratigraphic contacts (Long et al., 2011d; McQuarrie et al., 2008).

The sub-Himalaya in Bhutan are represented by the Siwalik Group, which comprises Miocene to Pliocene foreland sediments shed off the Himalaya (Bhargava, 1995; Coutand et al., 2016; Gansser, 1983). Siwalik sediments are bounded above by the MBT and below by the Main Frontal Thrust (MFT) (Figures 1 and 2).

*2.2 Structures*

The MCT is a continental-scale ductile shear zone with a top-to-the-south shear sense that was active during the Miocene, from ~24 to ~13 Ma (Chambers et al., 2011; Daniel et al., 2003; Godin et al., 2008, Martin, 2017; Tobgay et al., 2012). At the base of the GHS,

south-vergent shear bands filled with leucosomes yield monazite and xenotime U-Pb crystallization ages of 14–15 Ma, and a 1–2 km thick leucogranite sill is dated at 13.4 ± 0.2 Ma indicating that deformation within the GHS and along the MCT continued until at least 13 Ma (Daniel et al., 2003). The shear zone is several kilometers thick with diffuse boundaries, heterogeneous strain and variable degrees of mylonitization. We contend that the mapped MCT is a *protolith boundary* (sec. Schmid et al., 1987), although several protolith boundaries may exist within a crustal-scale shear zone (Schmid et al., 1987). For this reason, the nature of the MCT changes along the strike; the relatively sharp structural boundary in Bhutan is quite different from the km-wide ductile shear zone in Sikkim (Mottram et al., 2014a) or the relatively narrow zone of deformation in the Annapurna Himalaya (Parsons et al., 2016). We regard the pervasively sheared Jaishidanda Formation as a lithotectonic unit *within* the MCT mylonitic belt; its upper protolith boundary is the mapped MCT. Mylonitized Cambro-Ordovician granitoids of the GHS overlie the Jaishidanda Formation. Defining the upper boundary of the mylonitic belt is not possible because the entire GHS is sheared, and the gneisses are replaced by migmatites over a short structural distance (Daniel et al., 2003). The lower protolith boundary of the Jaishidanda Formation with the Shumar quartzites is either a stratigraphic discordance (Long et al., 2011c), a structural discordance caused by shearing within the MCT shear zone or a combination of both. According to the provenance criteria (Chakungal, 2006, Long et al., 2011c), we consider that the Jaishidanda Formation belongs stratigraphically to the GHS. The MCT mylonitic belt extends structurally downward for at least three kilometers, as documented by pervasive ductile deformation of quartzites with progressive changes in dynamic recrystallization mechanisms (Grujic et al., 1996; Long et al. 11c; Long et al. 2016; Starnes et al., 2020; this work). In addition, several bodies of mid-Proterozoic orthogneiss have been mapped within the Daling-Shumar Group (Gansser, 1983; Daniel et al., 2003, McQuarrie et al., 2019). Their contacts with metasedimentary rocks

are highly strained, characterized by mylonites and ultramylonites (McQuarrie et al., 2008; our field observations).

The GHS and Jaishidanda Formation are characterized by greenschist- to amphibolite-facies metamorphism, general strain ductile shearing, strong planar transposition and dominant subhorizontal lengthening and subvertical shortening (Long et al., 2016; our observations). The dominant planar fabric, subparallel to the MCT, is schistosity to gneissosity formed under peak metamorphic conditions (Agustsson et al., 2016; Chakungal, 2006; Daniel et al., 2003; Grujic et al., 1996; Warren et al., 2011). The deformation is pervasive, although heterogeneous, with the highest strain along the Jaishidanda–GHS protolith boundary (Daniel et al., 2003; Grujic et al., 1996, Long et al., 2016). The stretching lineation, mineral lineation and hinges of recumbent, tight to isoclinal folds, with the dominant foliation as axial planar foliation, all generally trend north-south (our observations). The shear sense is dominantly top-to-the-south, although at its top, the GHS is variably affected by a younger top-to-the-north shear fabric of normal-fault geometry within the South Tibetan Detachment system (Chambers et al., 2011; Kellett & Grujic, 2012; Kellett et al., 2013; Kellett et al., 2009; Kellett et al., 2010). The pure shear component with dominant vertical shortening is significant and variable (Corrie et al., 2012; Grujic et al., 1996; Grujic et al., 2002; Long, et al., 2011b; Long et al., 2011c; Long et al., 2016) and has been recognized elsewhere in the Himalaya (e.g., Grasemann et al., 1999; Larson & Godin, 2009; Law et al., 2004; Law et al., 2011).

In the Baxa Group, Diuri Formation and Gondwana sequence rocks, phyllitic cleavage, slaty cleavage (spaced smooth disjunctive to fine continuous) and axial planar, spaced cleavage to crenulation cleavage are found in fold hinges. In the Daling-Shumar Group, schist and phyllite dominate in the Daling Formation, and quartzite dominates in the Shumar Formation. The dominant planar fabric in the Daling Formation ranges from phyllitic

cleavage in the south to schistosity in the north, at a small angle to the lithological contact with quartzite. Bedding and compositional lamination are, however, preserved in quartzite, along with local tabular cross-bedding. Various kinematic indicators consistently show a top-to-the-south sense of shear (Grujic et al., 1996; Long et al., 2011c). Folds are inclined, open to isoclinal, with south vergence, and the kinematic criteria indicate top-to-the-south thrusting.

Few thrusts within the LHS are mappable, although several more are inferred in balanced cross sections (Long, et al., 2011a). The lower contact of the Daling-Shumar Group with the Baxa Group is always the Shumar thrust (Long et al., 2011d; McQuarrie et al., 2008; Ray et al., 1989), which is structurally similar to the Ramgarh thrust described farther west in Sikkim and Nepal (Bhattacharyya & Mitra, 2009; Shrestha et al., 1987a, 1987b; Srivastava & Mitra, 1994). For consistency with the related literature in Bhutan, however, we use the term Shumar thrust. The Diuri Formation is in stratigraphic contact above the Baxa Group in two localities, but all other contacts have been interpreted as tectonic (Long et al., 2011d). The upper contact of Gondwana sediments is a thrust with the Diuri Formation in its hanging wall, and the lower contact is the MBT (Figure 1).

Structural mapping and construction of detailed retro-deformable cross sections (Parui & Bhattacharyya, 2018; McQuarrie et al., 2008; Long et al., 2011a) indicate two lithotectonic units with different deformation styles within the LHS. The hanging wall of the Shumar thrust—the internal duplex—is characterized by a few horses forming a hinterland-dipping duplex arrangement in a brittle-ductile orogenic wedge (Figure 2). The top of this lithotectonic unit is the MCT (the LHS/GHS protolith boundary), but, as defined here, the MCT shear zone likely did not act as a "roof thrust", as in a critical Coulomb wedge. In addition, all the Daling-Shumar Group and Jaishidanda Formation rocks show pervasive ductile deformation, as evidenced by the presence of crystallographic preferred orientation

(CPO) in quartz and calcite mylonites and by dynamic recrystallization. The MCT ductile shear zone is the best explained by channel flow tectonics (Beaumont et al., 2006), according to which the MCT shear zone was the base of a Miocene south-flowing mid-crustal channel (Grujic 1996). The relation of this channel and the coeval upper crustal deformation or the role of the MCT in the extrusion and exhumation of this channel in the upper crust are outside the scope of this paper. The footwall of the Shumar thrust—the external duplex—is characterized by more but smaller horses in a hinterland-dipping duplex arrangement (Figure 2) with the MBT as the floor thrust and the Shumar thrust as the roof thrust. Klippen of Daling-Shumar rocks in eastern Bhutan (Figure 1, Long, et al., 2011a), the map relationships in the Sikkim-Darjeeling Himalaya (Bhattacharyya & Mitra, 2009; Parui & Bhattacharyya, 2018) and the burial temperatures presented here suggest that the Shumar thrust (or Ramgarh thrust in Sikkim) extended farther south. Along the strike of the eastern Himalaya, the geometry of this duplex varies greatly over distances of tens of kilometers (Long, et al., 2011a); locally, the horses are arranged into a hinterland-dipping duplex (as along our section), an antiformal stack to a foreland-dipping duplex (Bhattacharyya & Mitra, 2009; Parui & Bhattacharyya, 2018) or a combination (Long, et al., 2011a). Localized basal accretion in the external duplex led to significant local rock uplift, which in conjunction with focused surface erosion, formed tectonic windows, e.g., the Paro window in western Bhutan (Tobgay et al., 2012) and the Tista and Rangit windows in the Sikkim-Darjeeling Himalaya (Bhattacharyya & Mitra, 2009; Landry et al., 2016).

Farther south, the sub-Himalaya are deformed in the style of a foreland fold-and-thrust belt (i.e., critical Coulomb wedge) with thrusts and folds formed in a purely frictional setting. The floor thrust is the MFT, and the roof thrust, which behaves as a backstop, is the MBT (Hirschmiller et al., 2014).

The three main structures—MCT, MBT and MFT—merge at depth into the Main Himalayan Thrust (MHT) (Figure 2; Nelson et al., 1996), which is the basal detachment of the Himalaya.

### *2.2. Metamorphism*

Thermobarometric data for the LHS are available only for the Jaishidanda Formation rocks because of the absence of suitable mineral assemblages (e.g., garnet, biotite, plagioclase, or chlorite) in other LHS rocks. Metamorphic index mineral isograds, however, have been mapped (Gansser, 1983); these isograds indicate a northward increase in metamorphic grade and, together with the northward dip of the foliation, principal shear zones and tectonic boundaries, define an inverted metamorphic field gradient (Le Fort, 1975). In the LHS of eastern Bhutan, three metamorphic isograds were mapped by Gansser (1983): the "lower greenschist-facies" isograd stretching along the MBT, the "higher greenschist-facies" isograd in the upper Baxa Group, and the "biotite porphyroblast facies" isograd, which closely follows the trace of the MCT (Figure 1). At the structural level of the last isograd, within the Jaishidanda Formation, peak metamorphic mineral assemblages are interpreted to be garnet + biotite + muscovite + plagioclase + quartz, with peak metamorphic P-T conditions estimated in eastern Bhutan at ~650 ± 25 °C and 11-12 kbar (Daniel et al., 2003) and in central Bhutan at ~620 ± 25 °C (Long et al., 2016).

## 3 Geothermometry

### *3.1 Raman spectroscopy of carbonaceous material (RSCM)*

We apply two calibrations of the RSCM thermometer: (a) the one developed by Beyssac et al. (2002) for the temperature range from 330 °C to 650 °C because all the equivalent studies elsewhere in the LHS have used the same calibration and (b) the

calibration by Lahfid et al. (2010) and Rahl et al. (2005) for the temperature range from ~100 °C to 650 °C because many of our estimated temperatures are at the bottom range of the first calibration. Both RSCM thermometers use the same experimental setup and measured parameters (see Supporting Information Text S1 for details).

*3.1.1 Sample description and preparation*

Oriented carbonaceous material-bearing samples were collected from all lithological and tectonic units between the MCT and MBT (Figures 1 and 2; Table 1). The 19 samples are slates that contain disseminated fine-grained carbonaceous material.

All samples were cut perpendicular to foliation and perpendicular to the intersection and crenulation lineation to account for structural heterogeneities (Beyssac et al., 2002). Highly polished thick (30-100 μm) sections were prepared from these cuts. For samples with discrete graphite, the crystals were photographed using a reflected light microscope with a 50X objective, and the resulting photomicrographs were used to guide RSCM analyses (see Supporting Information Text S1 for details). When possible, at least 25 spots were measured in a sample to assure representative values (Aoya et al., 2010). In addition, we performed average Tukey's Biweight analysis (Press et al., 1992), in which the outlier values were ignored, and the reported temperatures were the mean values for coherent data. Temperature is reported with 2 standard errors of the mean (2 SEM), calculated as the quadratic addition of the 1σ internal error and external error of ± 50 °C from the calibration by Beyssac et al. (2002), divided by the square root of the number of analyses (n).

*3.1.2 Results*

The samples yield a set of Raman spectra for which the calculated mean temperatures range from ~340 to ~530 °C (Table 1, Figure 3). Since all the calculated temperatures are

>330 °C, the temperatures reported in the text and diagrams are calculated using the calibration by Beyssac et al. (2002); for discussion, see Lahfid et al. (2010). The LHS rocks in the footwall of the Shumar thrust exhibit uniformly low temperatures ranging from 337.0 ± 30.4 to 358.7 ± 31.7 °C, with a mean of 349.5 ± 8.1 °C (Figure 3a). Within the hanging wall of the Shumar thrust, LHS rocks yield a range of temperatures from bottom to top of the section from 438.1 ± 21.0 to 528.1 ± 22.5 °C (Figure 3b).

*3.2 Ti-in-quartz geothermobarometry*

Ti-in-quartz thermobarometry (TitaniQ) is based on the pressure and temperature (P-T) dependence of the solubility of titanium in quartz (Huang & Audetat, 2012; Kawasaki & Osanai, 2008; Ostapenko et al., 1987; Ostapenko et al., 2007; Thomas et al., 2010; Wark & Watson, 2006). The experiments by Thomas et al. (2015) confirm the calibration by Thomas et al. (2010), which is thus adopted for all temperature calculations in this paper.

To determine accurate temperatures, precise trace element measurements are coupled with microstructural observations, but two additional analyses should be applied:

(a) Determination of the pressure at which the temperature was acquired;

(b) Calculation of dynamic titania activity based on bulk rock chemistry.

However, the entire process must be iterative. In each analysis, the temperature is both the unknown and a required calculation parameter. To solve (a), thermokinematic modeling of multiple thermochronometric datasets may provide the most accurate pressure-temperature paths. To implement (b), the estimated temperature and pressure are input parameters to calculate the activity that returns a corrected temperature, which in turn is compared to the calculated P-T path to obtain a more accurate pressure.

*3.2.1 Sample description*

Over a structural distance of ~3000 m starting from the top at the Jaishidanda–GHS boundary (Figure 1), 11 samples of quartz tectonites were collected from the Jaishidanda and Shumar formations along a continuous roadside outcrop. All the samples display a mylonitic foliation and stretching lineation parallel to those of the MCT. Detailed studies of quartz microstructure were performed by (Grujic et al., 1996; Long et al., 2011c) and are not repeated here. The Jaishidanda and Shumar-Daling quartzites are characterized by grain boundary migration (GBM) recrystallization, which operates at temperatures between 500 and 700 °C (Stipp et al., 2002) or ~550-650 °C (Law, 2014). The quartz microstructure, however, exhibits 120° triple junctions and straight or gently curved grain boundaries characteristic of foam (Schmid, 1994) or partial-foam microstructure (Figure 4) associated with the switch to lower stress deformation (Kidder et al. 2016, and references therein). This microstructure is overprinted by progressive subgrain rotation (SGR) at deformation temperatures between 400 and 500 °C (Stipp et al., 2002) and ~450-550 °C (Law, 2014). Farther south, structurally down, Baxa Group quartzite often contains evidence for bulging recrystallization (Long et al., 2011c, Long et al., 2016) that corresponds to deformation temperatures between ~280 and 400 °C (Stipp et al., 2002) and 350-450 °C (Law, 2014). Active quartz slip systems determined from *a*- and *c*-axis distributions (Grujic et al., 1996) indicate both crossed girdle and single girdle fabrics and display the greatest concentrations of *c*-axis orientations at the division points of the *c*-axis cross girdles and lesser numbers at the center of the *c*-axis stereogram. Such topology indicates dominantly [r/z]<a> with minor contributions [m]<a> slip. This combined slip system coincides with SGR recrystallization, from ~400 to ~500 °C (Stipp et al., 2002). No brittle microstructure is observed; therefore, we infer that the shear along the MCT zone stopped before the deformation conditions reached the brittle-ductile transition.

Cathodoluminescence (CL) images of quartz provide qualitative information about growth and/or recrystallization histories (Bestmann & Pennacchioni, 2015; Morgan et al., 2014; Nachlas et al., 2014; Negrini et al., 2014). CL due to Ti is known to occupy the blue part of the spectrum in the region of 415 nm wavelength (Spear & Wark, 2009); however, comparisons between CL grayscale contrast and Ti concentration (Bestmann & Pennacchioni, 2015; Morgan et al., 2014) have shown that while in some cases Ti may be the main potential activator of the CL signal, in other cases, Ti is not the cause. Brightness contrasts in quartz CL textures (Figure 5) are sensitive to crystal lattice defects from recrystallization, and variations in trace element concentrations are secondary (e.g., Götze et al., 2004; Ramseyer et al., 1988). Therefore, in low-temperature quartz (i.e., low concentrations of Ti and other trace elements), CL zoning is dominated by lattice defects due to recrystallization (Watt et al., 1997). In the studied samples, the grain rims contain higher densities of subgrains and bulges.

*3.2.2 Analytical procedure*

All trace element measurements were performed on the sensitive high-resolution ion microprobe reverse-geometry (SHRIMP-RG) at Stanford University during four analytical sessions in 2010, 2012, 2013, and 2014 (see Supporting Information Text S2 for details).

The estimated 2σ uncertainty of the TitaniQ thermometer for the temperature range between 500 and 400 °C is ± 4–5 °C (Wark & Watson, 2006), while the analytical uncertainty for Ti measurements by SHRIMP-RG propagated into the geothermometer calibration is estimated to be ± 1–3 °C for the same temperature range (Grujic et al., 2011). Therefore, within-sample variations larger than ~10 °C are interpreted to reflect true temperature variations within the sample based on the standard deviation of replicate spot

analyses of the standard. The pressure of Ti-in-quartz equilibration and the effective $a_{TiO2}$ are defined in section 6.2.

*3.2.3 Bimodal Ti-in-quartz concentration*

Quartz rims have lower Ti concentrations, confirming that the Ti content correlates with the CL intensity (see section 3.2.1). Statistical analyses of all measurements also indicate a bimodal distribution of Ti concentrations in each sample (Table 2). For further discussion, we use the Ti concentrations of two peaks determined by kernel density estimation (Vermeesch, 2012). However, we must first determine the likely pressures at which the Ti concentrations were attained in the quartz grain core and rim and determine their respective $a_{TiO2}$ values (which also depend on pressure).

*3.2.4 Results*

Titania activities (Figure 6) were calculated following the modeling approach of Ashley and Law (2015) (see Supporting Information Text S2 and Tables S3 and S4 for details). For the initial presentation of the TitaniQ temperatures, we chose $a_{TiO2} = 1$ and the lowest pressure of 9 kbar (Table 2) determined for the metapelitic samples at the top of the transect (Daniel et al., 2003). The apparent temperature difference between the two data distribution peaks, corresponding to the CL bright cores and darker rims, is on the order of 10 °C (Table 2). The quartz grain cores yield ~50 °C lower temperatures than those obtained by the RSCM method at the same location. These are, however, not the final temperatures adopted in this paper, which are discussed after the pressure of Ti-in-quartz equilibration and the effective $a_{TiO2}$ are defined (section 6.2).

*3.3 Quartz c-axis fabric opening-angle thermometry*

Thin sections of 16 quartz-dominated samples (11 new samples and 5 samples reported in Grujic et al., 1996) were examined using a Russell-Head Instruments G60+ automated fabric analyzer at the University of British Columbia, Okanagan, to determine quartz *c*-axis orientations following the procedure described in (Larson, 2018), wherein one *c*-axis orientation was measured per quartz grain until a fabric of ~1000 individual measurements was generated. One exception to this methodology was sample BH 808, for which a grid of ~4000 points was used to determine the *c*-axis fabric. Previous studies using variations of this instrument design but employing the same principles yielded results indistinguishable from those generated using electron backscatter diffraction and X-ray texture goniometry (Peternell et al., 2010; Wilson et al., 2007).

Deformation temperatures were estimated from the opening angle of quartz *c*-axis fabrics (Figure 4) as measured based on contour diagrams produced using the program Orient (Vollmer, 2015). The use of this empirically derived thermometer assumed a lack of hydrolytic weakening and an invariant critically resolved shear stress (Kruhl, 1998; Morgan & Law, 2004). Fabric opening angles were converted to temperature using the pressure-independent calibration of Faleiros et al. (2016). Temperatures are reported with errors of ± 50 °C, which is intended to capture uncertainty in the determination of the opening angle and natural variation related to the previous assumptions (Faleiros et al., 2016; Kruhl, 1998; Law et al., 2004).

The obtained temperatures range from 390 to 600 °C (Table 3). These qualitative deformation temperature estimates are consistent with the corresponding RSCM temperatures but only marginally with the Ti-in-quartz temperatures. The final temperatures adopted in this paper are discussed after we define the pressure at which these temperatures were attained (section 6.2).

## 4 Muscovite $^{40}Ar/^{39}Ar$ Thermochronology

The dating of deformation or thermochronology in shear zones is an iterative process. Because the geothermal gradients and cooling and decompression rates are transient in time and diachronous in space (e.g., Coutand et al., 2014), the effective closure temperature and closure pressure (e.g., Liang, 2017) must be calculated for each point along a structural profile based on independent estimates of P-T conditions and cooling rates.

Muscovite was separated from five schist and gneiss samples adjacent to quartzite samples BH 133 and BH 804 for $^{40}Ar/^{39}Ar$ thermochronology (Figure 7). To obtain an internally consistent dataset, we also reanalyzed the data for four nearby samples originally reported by Long et al. (2012) and Stüwe & Foster (2001). No other samples could be analyzed because the Daling-Shumar rocks contain very fine-grained muscovite/illite, which could not be effectively separated from quartz. Muscovite defines the foliation in all samples and is interpreted as metamorphic. Muscovite grains are anhedral, and grain sizes range from ~0.5 mm to 3–5 mm. $^{40}Ar/^{39}Ar$ step heat thermochronology of muscovite separates was conducted at Dalhousie University (Halifax, Canada) using a Heine-based Ta double-vacuum furnace (see Supporting Information S1 for details). The data and plots are reported in Table 4 and Table S5 and Figure S1 in the supporting information. All ages are reported at the 2σ confidence level.

The structurally highest sample 11 from Stüwe & Foster (2001) is an orthogneiss (muscovite + biotite + quartz + plagioclase + K-feldspar) located approximately two kilometers above the MCT. Muscovite yielded a heterogeneous $^{40}Ar/^{39}Ar$ age spectrum. The inverse isochron plot shows a poorly-defined mixing line between atmospheric and radiogenic Ar. Excluding the final step (which plots off the array), the sample yields an inverse isochron age of 14.04 ± 0.4 Ma (MSWD = 6.2).

Two samples of the GHS orthogneiss in the immediate hanging wall of the MCT were collected one meter from the contact with the underlying Jaishidanda schists. Muscovite from BH 801 produced a saddle-shaped spectrum. Initial old steps are characteristic of excess Ar, final old steps may reflect excess or inherited Ar, and central steps define a plateau age of 11.76 ± 0.17 Ma. The inverse isochron plot shows a poorly-defined simple mixing line between atmospheric and radiogenic Ar with an age of 11.46 ± 0.45 Ma (MSWD = 8.2). The inverse isochron plot for equivalent sample 9 from Stüwe & Foster (2001) shows a poorly-defined mixing line between atmospheric and radiogenic Ar. Excluding the final step (which plots off the array) yields an isochron age of 11.70 ± 1.0 Ma (MSWD = 7.4).

Three samples from the Jaishidanda Formation were analyzed. Muscovite from sample BH 54 (garnet biotite muscovite schist) provided a saddle-shaped spectrum. The final old steps can arguably represent excess rather than inherited Ar, and steps 1100 °C and 1200 °C form an array toward highly radiogenic $^{40}Ar/^{39}Ar$. Excluding the steps with extraneous Ar (1, 2, 12-14), the remaining nine steps form a mixing line between atmospheric and radiogenic Ar with an age of 15.56 ± 0.60 Ma (MSWD = 4.1). Sample 8 from Stüwe & Foster (2001) is also a garnet two-mica schist, very likely from the same outcrop. The inverse isochron plot shows a mixing line between atmospheric and radiogenic Ar. Excluding the final step (which plots off the array) yields a well-defined inverse isochron age of 14.37 ± 0.48 Ma (MSWD = 0.57).

Muscovite from samples BH 802M (mica schist) and BH 802G (garnet schist), collected ~2 meters beneath sample BH 801, did not yield statistically significant plateaus. The inverse isochron plot for BH 802M shows a poorly-defined simple mixing line between atmospheric and radiogenic Ar with an age of 11.10 ± 0.87 Ma (MSWD = 6.0). In sample BH 802G, the initial old steps and downstepping staircase pattern may reflect excess Ar that diffused from the grain edge. The final old steps may reflect excess or inheritance. The

inverse isochron plot shows a poorly-defined simple mixing line between atmospheric and radiogenic Ar with an age of 11.70 ± 1.0 Ma (MSWD = 20.0).

Muscovite from BH 805, a sliver of mylonitic granitic gneiss within the Shumar quartzite ~600 m beneath the MCT, yields a well-defined plateau age of 12.18 ± 0.17 Ma. Including only the data that form an array between atmospheric and radiogenic Ar yields an inverse isochron age of 12.23 ± 0.39 Ma (MSWD = 4.7).

The lowest available sample, BU07-22 from Long et al. (2012), is a metasandstone from the Baxa Group in the footwall of the Shumar thrust. The inverse isochron plot is not particularly useful for this sample because it is highly radiogenic and there is no tie line near atmospheric $^{40}Ar/^{39}Ar$ to anchor the slope. Anchoring the first seven steps to $^{40}Ar/^{39}Ar = 298$ yields an inverse isochron age of ca. 15 Ma.

All the samples analyzed or reanalyzed in this study yield saddle-shaped spectra. The older steps indicate extraneous Ar that may be of excess (i.e., transported to the grain) or inherited (i.e., produced in situ) origin. The origins of the extraneous $^{40}Ar$ component are not resolvable using the inverse isochron plots because atmospheric $^{40}Ar$ accounts for such a large component of $^{40}Ar$ measured. We interpret the ages reported for the above samples as maximum reset or cooling ages affected by extraneous Ar.

The spectrum of sample BU07-22 is not saddle-shaped; the young initial steps and plateau followed by much older final steps indicate either partial inheritance of radiogenic Ar or a mixture of neocrystallized and incompletely reset detrital muscovite. The sample experienced the lowest metamorphic temperatures by far. The old ages, if due to inherited $^{40}Ar$, require that the muscovite be detrital, not metamorphic (Grujic et al., 2017). Thus, we would interpret these data to represent mixtures of detrital muscovite and neocrystallized metamorphic muscovite that grew below the closure T of muscovite for these conditions.

Muscovite Ar compositions and systematics in metamorphosed and deformed rocks can be challenging to deconvolve. There is potential for $^{40}Ar$ inheritance from incompletely degassed detrital or prograde metamorphic muscovite (non-open system behavior) (Mottram et al, 2015), uptake of excess $^{40}Ar$ (which should be abundant during metamorphism of old K-rich rocks such as the LHS and GHS) during cooling, changes to the diffusion domain size due to deformation (e.g., Cosca et al., 2011), and deformation-induced recrystallization during cooling (e.g., Mulch et al., 2005). In the case of this study, samples selected for $^{40}Ar/^{39}Ar$ analysis contain texturally metamorphic muscovite. The metamorphic temperatures of the dated samples are generally in the range of 425-550 °C (above the Shumar thrust), in which case the systems should have behaved as at least partly open if not fully open at the pressures estimated in this study (3-3.5 kbar), with respect to Ar (Warren et al., 2011). Sample BH 54 is the structurally lowest sample within the MCT shear zone and the sample most likely to have retained some inherited Ar and is therefore interpreted to reflect partial resetting of magmatic muscovite. Most of the dated samples show evidence of extraneous $^{40}Ar$, with much older initial and/or final age steps. We interpret this result to reflect the uptake of excess Ar during cooling (Kelley, 2002), and we argue that inheritance is unlikely, although we cannot rule it out entirely. The resulting interpreted ages are broadly consistent among the samples according to structural location and are consistent with both higher and lower temperature chronometers (monazite U-Pb and zircon U-Th/He); thus, we argue that the $^{40}Ar/^{39}Ar$ ages are representative of the cooling of these samples through the modeled closure temperature window of ~484 ± 25 °C. However, we do acknowledge that the lack of flat age spectra introduces uncertainty, which is why we report the ages as maximum reset or cooling ages.

To interpret the muscovite $^{40}Ar/^{39}Ar$ dates, we needed to independently determine the cooling rates and the pressures at which the local closure temperatures were attained. The

effective closure temperature for each sample was determined by iterative calculation using the pressure and the instantaneous cooling rate as predicted by thermokinematic modeling for each model "particle" at the corresponding location in the target temperature range.

## 5 Thermokinematic modeling

The 16 new and published muscovite $^{40}Ar/^{39}Ar$ thermochronometer ages are combined with four published apatite and 11 zircon (U-Th)/He and 37 apatite fission-track ages from Coutand et al. (2014) (Figure 7 and Table S6 in the supporting information) to perform formal inversions and assess the sensitivity of thermochronometric data to tectonic scenarios involving changing displacement rates on the MHT and various duplex-driven uplift processes. Although many more data are available for the region (Long et al., 2012, Coutand et al., 2014), the data were compiled along a relatively narrow, 25 km-wide swath (Figure 7) to avoid the influence of lateral structural variations in both the structures in the LHS (e.g., Long et al., 2011a; Long et al., 2012; McQuarrie et al., 2019) and the MHT itself (e.g., Singer et al., 2017). The inversions use the neighborhood algorithm (Rickwood & Sambridge, 2006; Sambridge, 1999) to select input values for the three-dimensional (3-D) thermokinematic model *Pecube* (Braun, 2003; Braun et al., 2012) and determine permissible ranges of geological parameters such as fault geometry, fault slip rate, crustal thermal properties, and the width, location and rate of duplex-induced accretion. Detailed descriptions of both the forward model *Pecube* (Braun et al., 2012) that we use, and the inversion procedure can be found in Coutand et al. (2014), Landry et al. (2016) and Supporting Information Text S3. The inversions were run on the cluster (ACEnet consortium) based at Dalhousie University and the geo-hpcc cluster at the University of Helsinki.

The aim of this modeling work is to determine the tectonothermal scenario that best reproduces the modern distribution of thermochronological ages across the Himalayan range

in eastern Bhutan. In addition to constraining the geometry of the basal detachment, the MHT, we extract the cooling histories of model particles in the MCT zone from 15-11 Ma to calculate more accurate closure temperatures for the applied thermochronometers and thermobarometers.

5.1 *Model design and input parameters*

In this paper, we utilize a three-stage tectonothermal scenario consistent with local geological data (Daniel et al., 2003) and previous modeling studies (e.g., Coutand et al., 2014; Long et al., 2012; McQuarrie et al., 2014, 2019, and references therein). This scenario involves a first stage from 15-11 Ma simulating the ongoing activity of the MCT after 13 Ma until the cessation of ductile shearing at 11 Ma (section 6.3, this study). A second stage starts at 11 Ma, during which the slip rate on the MHT changes after the MCT ceases activity and the MBT is activated. The duration of this second stage is not fixed and can last until from 7-2 Ma (we invert for this time and call it the "*transition time*" (*tt*). Furthermore, localized crustal accretion simulating duplex-enhanced uplift is also activated from 11 Ma onward. From the *tt* until the end of the simulations at 0 Ma, the kinematics of the MHT are again allowed to vary to reflect a potential partitioning of the India-Eurasia convergence between uplift of the Shillong Plateau and convergence at the Himalayan front (Biswas et al., 2007; Coutand et al., 2014, 2016).

The model domain extends from 26.5 to 28.5°N latitude and from 91 to 92.5°E longitude and thus has a surface extent of 165 × 220 km (Figure 8 summarizes the model design). The base of the model is 50 km below sea level, and the upper surface at the end of the simulations is defined using the modern topography. The modern topography is shifted at the start of the simulations such that lateral advection of the topography resulting from fault movement translates the model topography to its present-day location at 0 Ma (see Appendix

F of Coutand et al., 2014 for details). We note that some recent works have utilized an alternative approach to modelling topographic development in thermokinematic numerical models in Bhutan (McQuarrie and Ehlers, 2015; McQuarrie et al., 2019) where topography develops in response to fault-driven uplift with a defined elevation limit based on the taper angle of the topography across the Bhutanese Himalaya. While this approach has the benefit of simulating natural topographic growth, we have opted to utilize lateral translation of the modern topography because it is the simplest topographic treatment that ends with the present-day topography and includes its influence on the thermochronometer age data.

Although the MCT in eastern Bhutan was active by at least 23 Ma (Daniel et al., 2003), our simulations start at 15 Ma because the input thermochronological data are younger, providing constraints on crustal cooling after this time only. Furthermore, the thermal calculations evolve from a thermal steady state at the start of the simulations based on the model and fault geometries at 15 Ma, approximating the thermal field after 8 Myr of motion on the MCT. The thermal solutions begin at 15 Ma from a steady-state thermal solution calculated using the initial fault geometry, kinematics and modern topography (for details, see Braun et al., 2012). The subsequent transient thermal fields are calculated until the end of the run at 0 Ma, with a constant temperature boundary condition at the base of the model (see Table 5 for model parameters). Because in previous *Pecube* modeling studies, the average radiogenic heat production and the basal temperature were anticorrelated (Coutand et al., 2014; Landry et al., 2016), we fix the volumetric radiogenic heat production at an average value of 1.5 $\mu W/m^3$ (or 20 °C/Ma) and invert only for basal temperature in the range of 500-700 °C based on the estimates of upper mantle temperatures that must be less than ~600 °C to account for the seismicity (McKenzie et al., 2005; Priestley et al., 2008). This temperature is also consistent with those reported in previous thermokinematic (Hetényi et al., 2007) and geodynamic (Beaumont et al., 2004) modeling studies. Surface temperature decreases with

elevation at a lapse rate of 6 °C/km from 25 °C at sea level in the foreland (Naito et al., 2006).

Typical crustal values are used for rock properties in the model (Table 5). The MHT geometry is defined by coordinate pairs (X, Y) that mark changes in fault dip at a given horizontal distance from the fault surface trace and vertical distance from sea level. A constant India-Himalaya convergence rate of 17 mm/yr (Marechal et al., 2016) is used with partitioning factors λ that separate convergence into hanging wall overthrusting and footwall underthrusting (Figure 8). In the simulations in this work, we select three values for the partitioning factor reflecting the three different stages of the tested tectonomorphic scenario. 1) A low value of 0.25 between 15 and 11 Ma implies that 75% of the total convergence is accommodated by overthrusting on the MHT (~12.75 mm/yr). This low partitioning factor value increases heat advection toward the surface consistent with the ductile activity of the MCT at this time (Anczkiewicz et al., 2014; Daniel et al., 2003; Mottram et al., 2015). 2) A range of 0.5-0.9 is used after 11 Ma (cessation of activity of the MCT and activation of the MBT), and 3) we invert for a *tt* that corresponds to further slowing of the overthrusting rate along the MBT in eastern Bhutan between *x* and 0 Ma. In addition, a zone of enhanced rock uplift driven by basal accretion is activated after 11 Ma once duplex formation and activation of the MBT occur (McQuarrie & Ehlers, 2015, McQuarrie et al., 2019).

5.2 Modeling Results

A total of 20 sets of inversions were run in this study, but we present only the tectonothermal scenario described in section 5.1, which yields the lowest misfit value between observed and predicted thermochronological ages (Tables 5 and 6). This inversion set comprises 30,840 forward models with an excellent lowest misfit value of 0.46 (see

Coutand et al., 2014 for details about the misfit calculation). The values of related free parameters are found in Table 5 and Figure 9.

The geometry of the frontal (southern) part of the MHT is well constrained by independent geophysical and geological data (see points 1 to 5 in Figure 8 and Table 6; Hirschmiller et al., 2014; Singer et al., 2017; Coutand et al., 2014 and references therein), whereas the NA appraisal yields mostly flat one-dimensional posterior probability density functions (1-D PPDFs) with large 1σ errors for the depths of points 6 to 8 located in the northernmost part of the model (see $Z_6$, $Z_8$ and ($X_7$, $Z_7$) in Table 6 and Figures 7a-c and 8). This result indicates that despite the convergence of the inversion, these parameters remain relatively poorly resolved within the investigated ranges (Figure 9a-c). The basal temperature of approximately 550 °C that we obtain has a large 1σ error, but it is <600 °C and therefore consistent with the predicted Moho geotherm in this geotectonic setting (Mazzotti & Gueydan, 2018).

The NA appraisal stage indicates that the age dataset is most sensitive to the fault kinematics and the width and rate of basal accretion because the NA appraisal produces exponential and Gaussian 1-D PPDFs for these parameters (Figure 9). The partitioning factors $\lambda_2$ and $\lambda_3$ for the post-11 Ma stages of the model (decrease in the overthrusting rate on the MHT) are relatively well defined with values of 0.7 -0.1/+0.1 and 0.9 -0.1/+0.0, respectively, which correspond to overthrusting rates of 5.1 and 1.7 mm/a along the MHT. These values show that the data require a pronounced deceleration of overthrusting on the MHT after 11 Ma from the rate of 12.75 mm/a between 15 and 11 Ma, which partially agrees with other thermokinematic studies (McQuarrie & Ehlers, 2015, 2019). The *tt* between $\lambda_2$ and $\lambda_3$ remains poorly constrained at approximately 4.4 Ma but is compatible with approximately 5.9 Ma from the study by Coutand et al. (2014), which did not include muscovite $^{40}Ar/^{39}Ar$ data and localized basal accretion. Notably, $\lambda_2$ and the *tt* are strongly anticorrelated in the inversion, as are $\lambda_2$ and $\lambda_3$ to a lesser extent (Figure S2). The inversion produces a well-

defined 80 km-wide zone of basal accretion at a rate of 0.9 mm/a (Figure 9e-f) migrating southward during the last 11 Ma. Its southern margin is currently located 60 km north of the surface trace of the MFT and does not correspond to the location of the outer duplex (Figure 2; Long et al., 2011b; McQuarrie & Ehlers, 2015). This result suggests that the model cannot detect this structure, probably because exhumation was insufficient to impact the distribution of the high-temperature thermochronological data. At the current outcrop level, all white mica in the outer LHS rocks is detrital and only locally reset by Miocene metamorphism (Long et al., 2012; Grujic et al., 2017). Furthermore, the distribution of low-temperature thermochronological data is too sparse to constrain the models. For this reason, we are cautious about the interpretation of the RSCM data from the outer duplex but are confident in the interpretation of our observed and modeled data for the upper LHS because it was not affected by the outer duplex.

The parameters from the model with the lowest overall misfit were input into a high-resolution *Pecube* forward model to extract the predicted age data. Figure 10 shows an excellent fit between the predicted and measured ages for three thermochronometers. Subsequently, we used this forward model to calculate time-depth-temperature particle paths. Here, we focus on only the first stage of the tectonothermal scenario from 15-11 Ma, which corresponds to the period covered by the muscovite $^{40}Ar/^{39}Ar$ dates and to the MCT zone with RSCM and quartz thermobarometric data. The time-depth-temperature particle paths (Figure 11) are not linear because of the variable geometry of the basal detachment but generally indicate that the particles at the base of the studied section cooled through the same temperature approximately 1 Myr earlier than those at the top of the section. We use these paths to derive the cooling rates for the period covered by ages of a particular thermochronometer to more accurately estimate the closure temperature. For muscovite $^{40}Ar/^{39}Ar$ thermochronometry, deformation geothermometry and titania activity calculation,

which are all pressure dependent, we extract the pressure at the expected temperature to iteratively calculate the related temperatures discussed in the rest of this paper.

## 6 Discussion

### *6.1 Metamorphic temperature gradients in the MCT zone*

Seven of eight RSCM samples from the external (southern) duplex yield identical temperatures within uncertainty (Figures 2, 3a and S3). The external duplex is characterized by several horses, and the exhumation level is the same for all the measured samples (Figure 2; Long et al., 2011a, 2011b). Assuming a geothermal gradient of ~30 °C/km in the top 10 km of the crust (Figure 11c), a minimum Neogene burial depth of approximately 12 km is consistent with the geometry of the basal detachment in the area (Long et al., 2011b; McQuarrie & Ehlers, 2015; McQuarrie et al., 2019; Singer et al., 2017). All the metasedimentary rocks in the external duplex have Paleozoic depositional ages and likely did not experience any tectonic activity before Himalayan orogenesis; therefore, these temperatures might be Himalayan burial temperatures. Geological maps and cross sections in most of the Himalaya indicate that the GHS or even the Tethyan sedimentary sequence (Yu et al., 2015) extended significantly farther south than the current trace of the MCT; similarly, the Shumar thrust likely extended significantly farther south. Together, these thrust sheets and nappes may have provided tectonic burial that caused the Himalayan metamorphism of the Paleozoic rocks in the external duplex. The constant peak temperature for the 10 km of structural section between the MBT and Shumar thrust (Figure 3a) could have been produced by equally spaced hinterland-dipping horses, with nearly the same displacement and origins at the same crustal level (Figure 2; figure 3b in Long et al., 2012).

The 11 samples in the internal (northern) duplex are presented with their structural distance from the MCT rather than from the MBT because of the uncertain sequence of

deformation as well as underlying folds and duplexes (Figure 3b). Over 2.3 km of structural distance between the Shumar thrust and Jaishidanda Formation, the temperatures range from ~430 to ~530 °C (Figure 3b), yielding an apparent inverted temperature field gradient of 24.8 °C/km ($R^2$ = 0.9) (with error propagation in both temperature and structural location).

Similar temperature ranges between 330 °C and 580 °C have been obtained by RSCM in the LHS in central and western Nepal (Beyssac et al., 2004; Bollinger et al., 2004), NW Indian Himalaya (Célérier et al., 2009), and Arunachal Pradesh (Mathew et al., 2013). The inverted temperature gradients across the LHS estimated in these studies range from 25 to 50 °C/km. In central Bhutan, RSCM temperatures obtained by Long et al. (2016) range between 310 °C and 620 °C and up to 720 °C in the GHS, yielding a temperature gradient of approximately 270 °C/km (over approximately 1 km of structural distance across the MCT). One of the potential reasons for the difference in temperature gradients could be sample localization. Because different authors constructed various cross sections, the structural distances were not estimated consistently.

Furthermore, the mapped location of the MCT is not consistent among the various authors (for discussions on the topic, see Searle et al. (2008) and Martin (2017)). This location determines whether the highest temperature samples were included in the temperature field calculations. If we use the lowest RSCM temperature in the Shumar-Daling Group together with the thermobarometric data from Daniel et al. (2003), they would yield a gradient of approximately 70 °C/km, increasing to approximately 170 °C/km if we use the samples astride the MCT over a structural distance of 1.5 km (Figure 12). However, as discussed in section 6.3, these peak temperatures have different ages.

An alternative cause for the differences in temperature gradients obtained by RSCM is that graphite could have been affected by deformation (Kirilova et al., 2018, Kouketsu et al., 2019) or sample preparation (Kouketsu et al., 2019). The highest sample (BH 507) collected

from the Jaishidanda garnet schist ~2 meters beneath the GHS augen gneiss mylonite yields 446 ± 32 °C. This is the only sample with graphite; it has the highest error (Table 1), and the temperature is significantly lower than expected from the trends of the RSCM data, the opening-angle thermometry and the standard thermobarometry (Figure 12). The Ti-in-quartz temperature at the same structural level is also lower than expected from the trends of the same data (Figure 12). The most likely explanations for this discrepancy are that in sheared rocks, graphite thermometers may underestimate the peak metamorphic temperatures by up to 300 °C (Kirilova et al., 2018) and that the shearing caused by fault movement may lower graphite maturity (Kouketsu et al., 2019). We did not find evidence for brittle strain; thus, no evidence indicates that the last increments of deformation occurred at velocities sufficient to generate appreciable frictional heat. However, graphite is associated with muscovite, which is deformed by shearing and crenulation (Figure 4); therefore, graphite could be also deformed. We suggest that deformation under retrograde conditions (SGR recrystallization of large grains deformed by GBM recrystallization) outlasted the deformation toward the margin of the shear zone. In other words, the last stages of ductile shearing along the MCT were probably focused on a zone only tens of meters wide; therefore, any temperature gradient is apparent and is a finite result of the metamorphic and deformation history.

*6.2 Effective temperature of quartz recrystallization*

The quartz microstructure and texture indicate that dynamic recrystallization of the studied quartzite in the LHS occurred in the temperature range between ~400 and ~500 °C. The preliminary TitaniQ temperatures range between 400 and 470 °C (Table 2). The CL pattern and Ti-in-quartz concentrations indicate the core and rim microstructures of the quartz grains. The temperature differences obtained using the same $P$ and $a_{TiO2}$ for the core and rim are on the order of 10 °C. However, the pressure is unlikely to have remained constant during

cooling of the studied samples through this temperature range; it is thus plausible that the $a_{TiO2}$ changed as well (cf. Figures 6 and 10).

We address this problem by iteratively calculating the $a_{TiO2}$ and TitaniQ temperatures using the pressure at the expected temperature as predicted by thermokinematic modeling for each model "particle" at the corresponding location. The preliminary "expected temperature" is calculated by Ti-in-quartz thermometry not including the pressure parameter (Wark and Watson, 2006). Depth-temperature paths of the model particles from the region covering our field data indicate that Ti-in-quartz temperatures were reached at depths between approximately 10 and 14 km. From the work by Ashley and Law (2015) and our modeling of preliminary temperatures and pressures (Figure 6), we obtain $a_{TiO2}$ ~0.4. This value yields a more accurate temperature, in turn further constraining the pressure for each sample, which is inserted into the Ti-in-quartz thermobarometry equation including the pressure component (Thomas et a., 2010). The obtained temperature becomes the new "expected temperature". The process is repeated until both the pressure and temperature values converge. These are the Ti-in-quartz temperatures in the quartz cores shown in Figure 12 and used in further discussion. The quartz rim composition was acquired along the retrograde path accompanied by subgrain rotation recrystallization. Using the same iterative procedure, we obtain the deformation temperatures at which the quartz rims re-equilibrated during cooling and ongoing dynamic recrystallization (Figure 12).

Regardless of the accuracy of our temperature estimates, the rims of dynamically recrystallized quartz grains define an inverted temperature gradient, which indicates that the processes responsible for the inverted metamorphic sequence in the LHS were still operating during deformation under retrograde conditions until ~320 °C. Two samples collected within one meter from the contact with the GHS augen gneiss mylonite yield grain core temperatures approximately 25-50 °C lower than expected from the trend (Figure 12).

Equivalent to the trends of the RSCM temperatures, this result also indicates that ductile shearing in the core of the MCT shear zone outlasted the deformation toward the rim of the shear zone.

Although the modeled $a_{TiO2}$ value for some samples is 1 (Figure 6), the effective activities were probably lower. This feature is a result of the purity of the quartzites, where the lack of an appreciable amount of other oxide components ($Al_2O_3$, FeO, etc.) prevents the stabilization of other Ti-bearing phases in the thermodynamic models. This, in turn, forces the stability of rutile across P-T space; the predicted abundance of rutile is <0.1 volume % (see Table S4 in the supporting information). If this prediction is correct, then rutile would be disseminated throughout the sample in very small abundance, which would cause difficulties for achieving equilibrium at large distances from the rutile grains given the diffusive constraints on Ti buffering at these low temperatures (Ti is a high field strength element with sluggish diffusion at low temperatures). A more likely scenario is the presence of small amounts of biotite or white mica in the sample, which accommodate the trace amounts of bulk $TiO_2$ measured. Titania activity, if regulated by biotite under standard Barrovian metamorphic conditions, is typically <0.5 (Ashley & Law, 2015) and results in temperature estimates consistent with those for the other quartzite samples.

Observations (Grujic et al., 2011; Nachlas et al., 2014, this work) and experiments (Nachlas and Hirth, 2015; Negrini et al., 2014) reveal that Ti-in-quartz geothermometry is unlikely to register the peak deformation temperature in high-grade terranes (amphibolite facies and higher) if cooling is accompanied by ductile deformation. Investigation of the exact causes for this phenomenon is outside the aim of this paper, but the high diffusivity rates of Ti in quartz above 600 °C allow Ti to re-equilibrate fully and homogeneously to the retrograde conditions at the time scale of deformation under these temperatures. In contrast, sluggish diffusion rates of Ti at lower temperatures may cause partial re-equilibration with

the advantage of preserving synkinematic temperatures. The rate of Ti re-equilibration is dominated by volume diffusion rates if recrystallization is static (Cherniak et al., 2007; Thomas et al., 2015) or by the deformation mechanism type if recrystallization is dynamic (Grujic et al., 2011; Negrini et al., 2014). The observed Ti-in-quartz temperatures therefore also indicate that dynamic recrystallization continued with decreasing temperatures because at temperatures lower than ~400 °C, volume diffusion would require on the order of tens of million years to reset the concentrations of Ti in quartz to those corresponding to the measured temperatures in both the cores and rims. In the case of quartz mylonites in the MCT zone, this process occurred over 1-2 Myr.

*6.3 Timing for the inverted temperature gradient in the MCT zone*

The sample of Baxa quartzite in the immediate footwall of the Shumar thrust (Figure S4) yields mid-Proterozoic detrital zircon U-Pb ages with metamorphic overgrowths in the range of ~21 and ~14 Ma (Long et al., 2012, sample BU07-42). The weighted mean ages of 17.2 ± 0.3 Ma for the overgrowths and of the youngest three analyses of 14.9 ± 0.6 Ma were interpreted by Long et al. (2012) as revealing the times of motion along the Shumar thrust. Alternatively, these ages may be interpreted either as the times of metamorphism due to heating by the GHS nappe that extended farther south, close to the present surface trace of the MBT (Figure 2) or as the times of deformation enhancing fluid migration, which facilitated zircon crystallization. A sample of Baxa quartzite from the same structural level (Long et al., 2012, sample BU07-22) but located 30 km to the west yields a muscovite $^{40}Ar/^{39}Ar$ date of 15.28 ± 0.27 Ma (Figure S4), interpreted by Long et al. (2012) as the "structural burial" time of this sample by the Shumar thrust. However, this muscovite date should be interpreted cautiously, as Baxa quartzites contain detrital muscovite grains (in the Darjeeling Himalaya, they are all detrital; Grujic et al., 2017) and fine syndeformational white mica (Long et al.,

2012); therefore, the grain separates could have contained grains or fragments of both muscovite generations (Long et al., 2012, their figure 4d-e). In all LHS samples analyzed here, the muscovite grains are interpreted as metamorphic. In conclusion, and for further discussion, we assume that the motion along the Shumar thrust at approximately 450 °C was underway by approximately 15 Ma.

The effective muscovite $^{40}Ar/^{39}Ar$ closure temperature for each sample was determined by iterative calculation (Dodson, 1973) using the diffusion parameters from Harrison et al. (2008) and the pressure and instantaneous cooling rate as predicted by thermokinematic modeling for each model "particle" at the corresponding location and the target temperature range. Thus, estimated cooling rates in the MCT zone during the period corresponding to the temperature range of 600-300 °C were steady and linear, ranging from 78 to 91 °C/Ma, with a mean of 82 °C/Ma. Similar cooling rates, although from a different analysis of the thermochronological data, were inferred for western Bhutan (McQuarrie et al., 2014) and the Darjeeling Himalaya (Landry et al., 2016). According to thermokinematic models, cooling through the muscovite $^{40}Ar/^{39}Ar$ closure temperature range occurred at 12-13 km depth, i.e., at ~3.2-3.4 kbar, consistent with the thermobarometric data for the base of the GHS and the Jaishidanda Formation (Daniel et al., 2003). The effective closure temperature ($T_c$) of muscovite grains with radii larger than 0.5 mm is thus calculated to be approximately 484 °C using the Dodson equation (Dodson, 1973) and $^{40}Ar$ diffusion data at 5 kbar from (Harrison et al., 2009). For the GHS and Jaishidanda rocks, this temperature is retrograde; therefore, the muscovite $^{40}Ar/^{39}Ar$ dates are cooling ages. This $T_c$ is slightly lower at the top and somewhat higher at the bottom of the shear zone than the RSCM and quartz texture opening-angle temperatures, which we therefore interpret as having been established shortly before or after these muscovite $^{40}Ar/^{39}Ar$ dates. Ti-in-quartz temperatures are on the order of 100 °C lower

and ca. 1 Myr younger, based on modeling outputs, consistent with the calculated cooling rates.

Different ages (15.5 vs 11.5 Ma) from the same outcrop (BH 54 vs. Stu09) and same lithology (Jaishidanda schist) add complexity to the above interpretations. The $^{40}Ar/^{39}Ar$ age spectra obtained from mylonites frequently have staircase shapes (Kirschner et al., 1996). Muscovite grains from sample BH 54 (Figure S1) produce the most pronounced staircase $^{40}Ar/^{39}Ar$ age spectrum. One group of causes for such spectra are micas with different grain sizes, pre-existing and thermally overprinted micas, or a mixture of pre-existing and recrystallized micas. A combination of these muscovite microstructures was observed in sample BU07-22 by Long et al. (2012). We interpret these data as representing Cambrian detrital mica (Grujic et al., 2017) that partially reset at ~15.5 Ma. In this case, extraneous Ar in the final steps may be preserved components of a pre-existing "age reservoir".

A second possible explanation for the staircase $^{40}Ar/^{39}Ar$ age spectra is a single mica population that has undergone incomplete or partial diffusive argon loss. Empirical (Kirschner et al., 1996) and experimental (Cosca et al., 2011) work has demonstrated that $^{40}Ar$ loss can be induced by deformation and that micas are likely to preserve significant $^{40}Ar/^{39}Ar$ age variations and potentially record protracted time-temperature histories. All our samples are tectonites, and in all of them, muscovite crystals show evidence of plastic deformation, manifested as undulose extinction, crenulation, occasional kink bands, or muscovite blades damaged by shear bands (Figure 4). All samples with ~11 Ma populations include age steps at ~15 Ma (Figure S1). We have shown that the ductile deformation temperatures were below the ideal muscovite closure temperatures and thus tentatively suggest that the 11 Ma population reflects patchy $^{40}Ar$ loss induced by deformation below the muscovite $T_c$, while the ~15 Ma population indicates cooling through the ideal $T_c$ of ~480 °C. In summary, cooling of the MCT zone between ~500 and ~350 °C occurred from ~15 to ~11

Ma, and muscovite $^{40}Ar/^{39}Ar$ ages of ~11 Ma date the cessation of pervasive ductile deformation along the MCT. To more reliably distinguish between cooling and deformation ages, in situ UV-laser $^{40}Ar/^{39}Ar$ dating of muscovite in deformed rocks is necessary (e.g., Cosca et al., 2011, and references therein) yet remains analytically challenging for such young rocks.

The onset of slip along the Shumar thrust by 15 Ma (Long et al., 2012) with ongoing shearing along the MCT until ca. 11 Ma, as proposed here, is compatible because the two shear zones could have operated coevally. The transfer of deformation toward the foreland and progressive cessation of shearing along the pre-existing principal shear zone have been predicted by numerical experiments (e.g., Jaquet et al, 2018).

### *6.5 Kinematic models for the inverted temperature gradient in the footwall of an orogen-scale thrust*

Recent geochronological data indicate that the development of the inverted metamorphic sequence within the top of the LHS and the base of the GHS was progressive. In the Sikkim Himalaya, the tectonic unit corresponding to the Jaishidanda Formation is wider than that in Bhutan, allowing detailed investigation of the spatial trends of its pressure-temperature history. Lu-Hf garnet geochronology in this zone indicates downward younging of the onset of garnet growth and the timing of peak metamorphism (Anczkiewicz et al., 2014), varying from 14.6 ± 0.1 Ma in the sillimanite zone to 13.7 ± 0.2 Ma in the kyanite zone, 12.8 ± 0.3 Ma in the staurolite zone and 10.6 ± 0.2 Ma in the garnet zone. In western Bhutan, the prograde monazites are older in the north (~24 Ma) than in the south (~20 Ma; Tobgay et al., 2012), corresponding to downward younging of the prograde metamorphism within the GHS and the Jaishidanda Formation. However, monazite U-Th-Pb geochronology in Sikkim indicates that the peak of metamorphism along the same structural level is older in

the south than in the north—16 Ma vs. 10-9 Ma—presumably caused by the "progressive southward propagation of the slip" along the MCT (Mottram et al., 2015).

Our data from the upper LHS in eastern Bhutan indicate that neither the RSCM nor the quartz deformation temperatures correspond to the peak metamorphic temperatures, yet both define an inverted temperature gradient (Figure 12). We cannot explain this discrepancy for the RSCM data but suggest that the system can be reset by deformation at lower temperatures. The study by Kouketsu et al. (2019) raises serious concerns about sample preparation procedures because the preparation may lower the maturity of carbon grains, i.e., lower the apparent metamorphic temperature. We followed the measurement procedure outlined by Beyssac et al. (2002); therefore, our RSCM data should be comparable to other published RSCM data in the Himalaya. The small scatter of data within a sample and the clear temperature trends make us confident that the results are real rather than laboratory artifacts. The deformation of graphite or carbon microstructure and the lowering of graphite crystallinity due to shearing caused by fault movement (Kirilova et al., 2018; Kouketsu et al., 2019) could explain the lower than expected temperature of sample BH 507 closest to the contact the Jaishidanda schists and GHS gneisses. However, our RSCM temperatures are in the same range as those from all other studies in the Himalaya. For the quartz tectonites, the microstructures indicate replacement of higher temperature microstructures by colder microstructures. Reworking of the high-T microstructure (GBM recrystallization) by low-T shearing (SGR recrystallization) is consistent with the reduction in temperature over time. Furthermore, because pervasive ductile deformation persisted under decreasing temperatures and during 2-4 Myr, the high-temperature information locked in the minerals was deformed as a passive strain marker. This interpretation implies that a peak-temperature profile across a crustal-scale shear zone is a finite strain feature.

Pervasive ductile shear within the sequence and along the MCT shear zone emplaced hot rocks over colder rocks, overturning the synkinematic isotherms at the mid-crustal level (e.g., Beaumont et al., 2004); peak-temperature isotherms (if preserved in the rock record) were subsequently sheared and variably overprinted by ongoing ductile shear under retrograde conditions. A fine example of such a process was documented by Williams and Platt (2017) in the Alborán Domain, southern Spain.

Thermokinematic modeling (Bollinger et al., 2006, Célérier et al., 2009; Herman et al., 2010, Coutand et al., 2014; Landry et al., 2016) and sequential restoration of balanced cross sections guided by thermokinematic modeling (McQuarrie and Ehlers, 2015; 2019) show that thermochronological data obtained from the LHS can be well fit by a two-stage evolutionary scenario: an early-middle Miocene phase that involved thrusting of a hot hanging wall over a downgoing footwall and the later formation of the external duplex by basal accretion. To reconcile our microstructural, thermobarometric, and thermochronologic observations with the experimental data, we suggest that the pervasive ductile deformation along the MCT zone stopped at ~11 Ma when the deformation focused fully within the external LHS duplex.

In such a dynamic crustal system, there is no steady thermal state or steady and unique cooling path of the rocks. The material points at different structural levels attain their respective peak temperatures at different times. Such progressive changes in deformation temperatures are recorded by deformation temperatures acquired by Ti-in-quartz thermobarometry. The dynamically recrystallized quartz grains did not record peak temperatures in the upper LHS. The quartz continued to deform under decreasing temperatures and re-equilibrate the Ti-in-quartz concentrations until ~320 °C, at which point crystal plastic deformation stopped.

Muscovite samples covering the range of the Ti-in-quartz samples indicate a muscovite $^{40}Ar/^{39}Ar$ age trend. Across the MCT shear zone, there is an upward-younging muscovite

$^{40}Ar/^{39}Ar$ age trend; accordingly, the quartz deformation temperatures may be progressively younger down section. According to the time-temperature paths (Figure 11), cooling through the same temperature occurred approximately half a million years later at the protolith boundary than three kilometers below it. There remain uncertainties in the interpretation of Ar/Ar data for metamorphic muscovite such as those used in this study. Further corroboration of these results using complementary thermochronometers (e.g. apatite U-Pb) and/or along parallel transects would be beneficial to test these interpretations. This age difference across the shear zone is small yet may have important implications. The footwall samples away from the core of a crustal-scale shear zone cool earlier; thus, the dominant deformation mechanisms change earlier. Because lower temperature deformation mechanisms require higher flow stresses at the same strain rate, a shear zone most likely progressively narrows during cooling. Strain localization in the central part of a shear zone typifies Type 2 shear zones (e.g., Fossen & Cavalcante, 2017). Moreover, strain analyses indicate that the finite strain registered by quartz porphyroclasts (retrograde strain) increases toward the MCT (Long et al., 2016; Starnes et. al., 2020). In contrast, geochronological data linked to the peak metamorphic assemblages (Mottram et al., 2015) indicate shear zone widening and Type 1 shear zones.

These observations highlight the important fact that crustal-scale dip-slip shear zones evolve over long geologic intervals, during which temperature and pressure conditions change. In the prograde stage, the shear zone widens by wall rock weakening mechanisms, while in the retrograde stage, shear zones narrow, and flow stresses increase (see, e.g., Fossen & Cavalcante, 2017; Jaquet and Schmalholz 2018, and references therein).

## 7 Conclusions

The spatial distributions of metamorphic and deformation temperatures indicate that a synkinematic inverted temperature field gradient was present between ~20 Ma and 11 Ma and was progressively deformed at all stages of ductile deformation.

The spatial pattern of temperatures across the Lesser Himalayan Sequence (LHS), acquired by Raman spectroscopy on carbonaceous materials, indicates two temperature sequences. The external temperature sequence has a flat profile; i.e., peak temperatures are the same across 10 km of the structural sequence. The internal temperature sequence in the MCT shear zone shows an inverted temperature field gradient, from ~450 to ~530 °C, yielding an apparent temperature/structural distance gradient of approximately 12 °C/km. The same temperature gradient in the MCT shear zone is obtained by the deformation thermometry based on quartz *c*-axis fabrics. The Ti-in-quartz thermobarometry, however, yields significantly lower temperatures. The resetting of the Ti concentration in quartz in the observed temperature range and time span could have been achieved only by crystal plastic processes. This interpretation is consistent with the observed quartz microstructure. Because the muscovite blades in the same mylonites are deformed, we interpret the 11 Ma muscovite $^{40}Ar/^{39}Ar$ dates as the age of the last ductile increment along the MCT in eastern Bhutan.

To constrain the age of related deformation or better, the time span of ductile deformation under retrograde conditions, the most reliable thermochronological tool is likely in situ UV-laser $^{40}Ar/^{39}Ar$ dating of muscovite in deformed rocks (Cosca et al., 2011; Kellett et al., 2016; Mulch & Cosca, 2004). However, it is doubtful this could be done on Neogene muscovite, which would not yield sufficient radiogenic $^{40}Ar$ to be sampled at a high enough spatial resolution.

The inverted metamorphic field gradient is registered by various geothermometric systems and at different temperature ranges, indicating that the processes that formed the

currently exposed (i.e., finite) metamorphic gradient endured over an extended geological interval along the retrograde metamorphic path and involved various processes at different stages:

(a) Synkinematic steepening and inversion of the isotherms in the vicinity of the crustal-scale shear zone;

(b) Locking in of the peak-*T* isotherms recorded by the metamorphic assemblages;

(c) Ongoing pervasive ductile deformation characterized by general shear (both simple and pure shear components);

(d) Deformation of the peak-*T* isotherms and formation of the quartz deformation isotherms;

(e) Deformation focusing (progressive shear zone narrowing) that may have further deformed the peak-*T* isotherms.

**Acknowledgments**

Readers can access the new thermochronological data at the following sources:

Raman spectroscopy on carbonaceous material in Bhutan,

https://doi.org/10.26022/IEDA/111507

Ti-in quartz thermobarometry for Bhutan quartz mylonites,

https://doi.org/10.26022/IEDA/111508

Bhutan Muscovite 40Ar/39Ar thermochronology - 2020-02-24,

https://doi.org/10.26022/IEDA/111509

Critical comments by Aaron Martin, Sean Long and two anonymous reviewers and by the Associate Editor, Peter van der Beek greatly helped to improve our work. The study was supported by the Natural Sciences and Engineering Research Council of Canada (NSERC)

grants RGPIN/227475-2009 and RGPIN/4297-2014, and the National Science Foundation (USA). Fieldwork in the Kingdom of Bhutan was enabled by the invaluable help provided by the people and the Royal Government of Bhutan, and by the Hoch family.

## References

Adlakha, V., Lang, K. A., Patel, R. C., Lal, N., & Huntington, K. W. (2013). Rapid long-term erosion in the rain shadow of the Shillong Plateau, Eastern Himalaya. *Tectonophysics, 582*, 76-83. http://dx.doi.org/10.1016/j.tecto.2012.09.022

Agustsson, K., Gordon, S., Long, S., Seward, G., Zeiger, K., & Penfold, M. (2016). Pressure–temperature–structural distance relationships within Greater Himalayan rocks in eastern Bhutan: implications for emplacement models. *Journal of Metamorphic Geology, 34*(7), 641-662.

Anczkiewicz, R., Chakraborty, S., Dasgupta, S., Mukhopadhyay, D., & Koltonik, K. (2014). Timing, duration and inversion of prograde Barrovian metamorphism constrained by high resolution Lu-Hf garnet dating: A case study from the Sikkim Himalaya, NE India. *Earth and Planetary Science Letters, 407*, 70-81.

Aoya, M., Kouketsu, Y., Endo, S., Shimizu, H., Mizukami, T., Nakamura, D., & Wallis, S. (2010). Extending the applicability of the Raman carbonaceous-material geothermometer using data from contact metamorphic rocks. *Journal of Metamorphic Geology, 28*(9), 895-914. http://doi.wiley.com/10.1111/j.1525-1314.2010.00896.x

Ashley, K. T., & Law, R. D. (2015). Modeling prograde TiO2 activity and its significance for Ti-in-quartz thermobarometry of pelitic metamorphic rocks. *Contributions to Mineralogy and Petrology, 169*(2), 1-7.

Barman, P., Jade, S., Shrungeshwara, T., Kumar, A., Bhattacharyya, S., Ray, J. D., et al. (2016). Crustal deformation rates in Assam Valley, Shillong Plateau, Eastern Himalaya, and Indo-Burmese region from 11 years (2002–2013) of GPS measurements. *International Journal of Earth Sciences*, 1-14.

Beaumont, C., Jamieson, R. A., Nguyen, M. H., & Medvedev, S. (2004). Crustal channel flows: 1. Numerical models with applications to the tectonics of the Himalayan-Tibetan orogen. *Journal Of Geophysical Research-Solid Earth, 109*(B6), B06406.

Bestmann, M., & Pennacchioni, G. (2015). Ti distribution in quartz across a heterogeneous shear zone within a granodiorite: The effect of deformation mechanism and strain on Ti resetting. *Lithos, 227*, 37-56.

Beyssac, O., Bollinger, L., Avouac, J. P., & Goffé, B. (2004). Thermal metamorphism in the lesser Himalaya of Nepal determined from Raman spectroscopy of carbonaceous material. *Earth and Planetary Science Letters, 225*(1-2), 233-241.

Beyssac, O., Goffé, B., Chopin, C., & Rouzaud, J. N. (2002). Raman spectra of carbonaceous material in metasediments: a new geothermometer. *Journal of Metamorphic Geology, 20*(9), 859-871.

Bhargava, O. N. (Ed.) (1995). *The Bhutan Himalaya: a geological account* (Vol. 39).

Bhattacharyya, K., & Mitra, G. (2009). A new kinematic evolutionary model for the growth of a duplex - an example from the Rangit duplex, Sikkim Himalaya, India. *Gondwana Research, 16*(3-4), 697-715.

Bollinger, L., Avouac, J. P., Beyssac, O., Catlos, E. J., Harrison, T. M., Grove, M., et al. (2004). Thermal structure and exhumation history of the Lesser Himalaya in central Nepal. *Tectonics, 23*(5).

Bollinger, L., Henry, P. and Avouac, J.P. (2006.) Mountain building in the Nepal Himalaya: Thermal and kinematic model. *Earth and Planetary Science Letters, 244*(1-2), 8-71. https://doi.org/10.1016/j.epsl.2006.01.045.

Braun, J. (2003). Pecube: a new finite-element code to solve the 3D heat transport equation including the effects of a time-varying, finite amplitude surface topography. *Computers & Geosciences, 29*(6), 787-794.

Braun, J., Van Der Beek, P., Valla, P., Robert, X., Herman, F., Glotzbach, C., et al. (2012). Quantifying rates of landscape evolution and tectonic processes by thermochronology and numerical modeling of crustal heat transport using PECUBE. *Tectonophysics, 524-525*, 1-28.

Caddick, M. J., Bickle, M. J., Harris, N. B. W., Holland, T. J. B., Horstwood, M. S. A., Parrish, R. R., & Ahmad, T. (2007). Burial and exhumation history of a Lesser Himalayan schist: Recording the formation of an inverted metamorphic sequence in NW India. *Earth and Planetary Science Letters, 264*(3-4), 375-390.

Célérier, J., Harrison, T., Beyssac, O., Herman, F., Dunlap, W., & Webb, A. (2009). The Kumaun and Garwhal Lesser Himalaya, India: Part 2. Thermal and deformation histories. *Geological Society of America Bulletin, 121*(9-10), 1281.

Chakungal, J. (2006). *Geochemistry and metamorphism of metabasites, and spatial variation of P-T paths across the Bhutan Himalaya: implications for the exhumation of the Greater Himalayan Sequence.* (Ph.D. Ph.D.), Dalhousie University, Halifax.

Chambers, J., Parrish, R., Argles, T., Harris, N., & Horstwood, M. (2011). A short-duration pulse of ductile normal shear on the outer South Tibetan detachment in Bhutan: Alternating channel flow and critical taper mechanics of the eastern Himalaya. *Tectonics, 30*(TC2005).

Cherniak, D. J., Watson, E. B., & Wark, D. A. (2007). Ti diffusion in quartz. *Chemical Geology, 236*(1-2), 65-74.

Cooper, F. J., Hodges, K. V., & Adams, B. A. (2012). Metamorphic constraints on the character and displacement of the South Tibetan fault system, central Bhutanese Himalaya. *Lithosphere, 5*(1), 67-81. http://lithosphere.gsapubs.org/cgi/doi/10.1130/L221.1

Corrie, S. L., Kohn, M. J., McQuarrie, N., & Long, S. P. (2012). Flattening the Bhutan Himalaya. *Earth and Planetary Science Letters, 349-350*(C), 67-74. http://dx.doi.org/10.1016/j.epsl.2012.07.001

Cosca, M., Stünitz, H., Bourgeix, A.-L., & Lee, J. P. (2011). 40Ar* loss in experimentally deformed muscovite and biotite with implications for 40Ar/39Ar geochronology of naturally deformed rocks. *Geochimica et Cosmochimica Acta, 75*(24), 7759-7778.

Coutand, I., Barrier, L., Govin, G., Grujic, D., Hoorn, C., Dupont-Nivet, G., & Najman, Y. (2016). Late Miocene-Pleistocene evolution of India-Eurasia convergence partitioning between the Bhutan Himalaya and the Shillong Plateau: New evidences from foreland basin deposits along the Dungsam Chu section, eastern Bhutan. *Tectonics, 35*(12), 2963-2994.

Coutand, I., Whipp, D. M., Grujic, D., Bernet, M., Fellin, M. G., Bookhagen, B., et al. (2014). Geometry and kinematics of the Main Himalayan Thrust and Neogene crustal exhumation in the Bhutanese Himalaya derived from inversion of multithermochronologic data. *Journal Of Geophysical Research-Solid Earth, 119*(2), 1446-1481.

Daniel, C. G., Hollister, L. S., Parrish, R. R., & Grujic, D. (2003). Exhumation of the Main Central Thrust from lower crustal depths, Eastern Bhutan Himalaya. *Journal of Metamorphic Geology, 21*(4), 317-334.

Dasgupta, S. (1995). Jaishidanda Formation. In O. N. Bhargava (Ed.), *The Bhutan Himalaya: A Geological Account* (Vol. 39, pp. 79-88): Geological Survey of India.

Davidson, C., Grujic, D. E., Hollister, L. S., & Schmid, S. M. (1997). Metamorphic reactions related to decompression and synkinematic intrusion of leucogranite, High Himalayan Crystallines, Bhutan. *Journal of Metamorphic Geology, 15*(5), 593-612.

Dodson, M. H. (1973). Closure temperature in cooling geochronological and petrological systems. *Contribution to Mineralogy and Petrology, 40*(40), 259-274.

Faleiros, F. M., Moraes, R. d., Pavan, M., & Campanha, G. A. d. C. (2016). A new empirical calibration of the quartz c-axis fabric opening-angle deformation thermometer. *Tectonophysics, 671*, 173-182.

Fossen, H., & Cavalcante, G. C. G. (2017). Shear zones–A review. *Earth-Science Reviews, 171*, 434-455.

Gaidies, F., Petley-Ragan, A., Chakraborty, S., Dasgupta, S., & Jones, P. (2015). Constraining the conditions of Barrovian metamorphism in Sikkim, India: P-T-t paths of garnet crystallization in the Lesser Himalayan Belt. *Journal of Metamorphic Geology, 33*(1), 23-44.

Gansser, A. (1983). *Geology of the Bhutan Himalaya* (Vol. 96). Basel-Boston-Stuttgart: Birkhäuser Verlag.

Gilmore, M. E., McQuarrie, N., Eizenhöfer, P. R., & Ehlers, T. A. (2018). Testing the effects of topography, geometry, and kinematics on modeled thermochronometer cooling ages in the eastern Bhutan Himalaya. *Solid Earth, 9*(3), 599.

Goscombe, B., Gray, D., & Foster, D. A. (2018). Metamorphic response to collision in the Central Himalayan Orogen. *Gondwana Research, 57*, 191-265.

Götze, J., Plötze, M., Graupner, T., Hallbauer, D. K., & Bray, C. J. (2004). Trace element incorporation into quartz: A combined study by ICP-MS, electron spin resonance, cathodoluminescence, capillary ion analysis, and gas chromatography. *Geochimica et Cosmochimica Acta, 68*(18), 3741-3759. http://www.sciencedirect.com/science/article/pii/S0016703704000353

Grasemann, B., Fritz, H., & Vannay, J. C. (1999). Quantitative kinematic flow analysis from the Main Central Thrust Zone (NW-Himalaya, India): implications for a decelerating strain path and the extrusion of orogenic wedges. *Journal of Structural Geology, 21*(7), 837-853.

Groppo, C., Rolfo, F., & Lombardo, B. (2009). P-T Evolution across the Main Central Thrust Zone (Eastern Nepal): Hidden Discontinuities Revealed by Petrology. *Journal of Petrology, 50*(6), 1149-1180

Grujic, D., Casey, M., Davidson, C., Hollister, L. S., Kündig, R., Pavlis, T., & Schmid, S. (1996). Ductile extrusion of the Higher Himalayan Crystalline in Bhutan: Evidence from quartz microfabrics. *Tectonophysics, 260*(1-3), 21-43.

Grujic, D., Stipp, M., & Wooden, J. L. (2011). Thermometry of quartz mylonites: Importance of dynamic recrystallization on Ti-in-quartz reequilibration. *Geochemistry Geophysics Geosystems, 12*(6), Q06012. /doi.org/10.1029/2010GC003368

Grujic, D., Coutand, I., Doon, M., & Kellett, D. A. (2017). Northern provenance of the Gondwana Formation in the Lesser Himalayan Sequence: constraints from 40Ar/39Ar dating of detrital muscovite in Darjeeling-Sikkim Himalaya. *Italian Journal of Geosciences, 136*(1), 15-27.

Grujic, D., Govin, G., Barrier, L., Bookhagen, B., Coutand, I., Cowan, B., et al. (2018). Formation of a Rain Shadow: O and H Stable Isotope Records in Authigenic Clays From the Siwalik Group in Eastern Bhutan. *Geochemistry, Geophysics, Geosystems*.

Grujic, D., Hollister, L. S., & Parrish, R. R. (2002). Himalayan metamorphic sequence as an orogenic channel: insight from Bhutan. *Earth and Planetary Science Letters, 198*(1-2), 177-191.

Grujic, D., Stipp, M., & Wooden, J. L. (2011). Thermometry of quartz mylonites: Importance of dynamic recrystallization on Ti-in-quartz reequilibration. *Geochemistry Geophysics Geosystems, 12*(6), Q06012.

Godin, L., Grujic, D., Law, R., & Searle, M. (2006). Channel flow, ductile extrusion and exhumation in continental collision zones: an introduction. *Geological Society London Special Publications*. http://sp.lyellcollection.org/cgi/content/abstract/268/1/1

Goscombe, B., Gray, D. and Foster, D.A., 2018. Metamorphic response to collision in the Central Himalayan Orogen. *Gondwana Research*, *57*, pp.191-265. https://doi.org/10.1016/j.gr.2018.02.002.

Harrison, T. M., Célérier, J., Aikman, A. B., Hermann, J., & Heizler, M. T. (2009). Diffusion of 40Ar in muscovite. *Geochimica et Cosmochimica Acta, 73*(4), 1039-1051. http://linkinghub.elsevier.com/retrieve/pii/S0016703708006819

Herman, F., Copeland, P., Avouac, J.P., Bollinger, L., Mahéo, G., Le Fort, P., Rai, S., Foster, D., Pêcher, A., Stüwe, K. and Henry, P. (2010), Exhumation, crustal deformation, and thermal structure of the Nepal Himalaya derived from the inversion of thermochronological and thermobarometric data and modeling of the topography, J. Geophys. Res., 115, B06407, doi:10.1029/ 2008JB006126.

Hetényi, G., Cattin, R., Brunet, F., Bollinger, L., Vergne, J., Nábělek, J. L., & Diament, M. (2007). Density distribution of the India plate beneath the Tibetan plateau: Geophysical and petrological constraints on the kinetics of lower-crustal eclogitization. *Earth and Planetary Science Letters, 264*(1-2), 226-244. http://linkinghub.elsevier.com/retrieve/pii/S0012821X0700605X

Hirschmiller, J., Grujic, D., Bookhagen, B., Coutand, I., Huyghe, P., Mugnier, J.-L., & Ojha, T. (2014). What controls the growth of the Himalayan foreland fold-and-thrust belt? *Geology*, *42*(3), 247-250.

Huang, R. F., & Audetat, A. (2012). The titanium-in-quartz (TitaniQ) thermobarometer: A critical examination and re-calibration. *Geochimica et Cosmochimica Acta, 84*(C), 75-89.

Jaquet, Y. and Schmalholz, S.M. (2018). Spontaneous ductile crustal shear zone formation by thermal softening and related stress, temperature and strain rate evolution. *Tectonophysics*, *746*, 384-397.

Jaquet, Y., Duretz, T., Grujic, D., Masson, H., & Schmalholz, S. M. (2018). Formation of orogenic wedges and crustal shear zones by thermal softening, associated topographic evolution and application to natural orogens. *Tectonophysics, 746*, 512-529.

Kawasaki, T., & Osanai, Y. (2008). Empirical thermometer of $TiO_2$ in quartz for ultrahigh-temperature granulites of East Antarctica. In M. Satish-Kumar, Y. Motoyoshi, Y. Osanai, Y. Hiroi, & K. Shiraishi (Eds.), *Geodynamic evolution of East Antarctica* (Vol. 308, pp. 419-430).

Kellett, D. A., & Grujic, D. (2012). New insight into the South Tibetan detachment system: Not a single progressive deformation. *Tectonics, 31*(2), https://agupubs.onlinelibrary.wiley.com/doi/pdf/10.1029/2011TC002957

Kellett, D. A., Grujic, D., Coutand, I., Cottle, J., & Mukul, M. (2013). The South Tibetan detachment system facilitates ultra rapid cooling of granulite-facies rocks in Sikkim Himalaya. *Tectonics*, *32*(2), 252-270.

Kellett, D. A., Grujic, D., & Erdmann, S. (2009). Miocene structural reorganization of the South Tibetan detachment, eastern Himalaya: Implications for continental collision. *Lithosphere, 1*(5), 259-281.

Kellett, D. A., Grujic, D., Warren, C., Cottle, J., Jamieson, R., & Tenzin, T. (2010). Metamorphic history of a syn-convergent orogen-parallel detachment: The South Tibetan detachment system, Bhutan Himalaya. *Journal of Metamorphic Geology, 28*(8), 785-808.

Kellett, D. A., Warren, C., Larson, K. P., Zwingmann, H., van Staal, C. R., & Rogers, N. (2016). Influence of deformation and fluids on Ar retention in white mica: Dating the Dover Fault, Newfoundland Appalachians. *Lithos, 254*, 1-17.

Kidder, S., Hirth, G., Avouac, J.-P., & Behr, W. (2016). The influence of stress history on the grain size and microstructure of experimentally deformed quartzite. *Journal of Structural Geology, 83*, 194-206.

Kirilova, M., Toy, V., Rooney, J. S., Giorgetti, C., Gordon, K. C., Collettini, C., & Takeshita, T. (2018). Structural disorder of graphite and implications for graphite thermometry. *Solid Earth, 9*(1).

Kirschner, D. L., Cosca, M. A., Masson, H., & Hunziker, J. C. (1996). Staircase 40/Ar39Ar spectra of fine-grained white mica: Timing and duration of deformation and empirical constraints on argon diffusion. *Geology, 24*(8), 747-750.

Kohn, M. J. (2014). Himalayan metamorphism and its tectonic implications. *Annual Review of Earth and Planetary Sciences, 42*, 381-419.

Kohn, M. J., Catlos, E. J., Ryerson, F. J., & Harrison, T. M. (2001). Pressure-temperature-time path discontinuity in the Main Central Thrust zone, central Nepal. *Geology, 29*, 571– 574.

Kouketsu, Y., Miyake, A., Igami, Y., Taguchi, T., Kagi, H., & Enami, M. (2019). Drastic effect of shearing on graphite microtexture: attention and application to Earth science. *Progress in Earth and Planetary Science, 6*(1), 1-12.

Kruhl, J. (1998). Prism-and basal-plane parallel subgrain boundaries in quartz: a microstructural geothermobarometer. Reply. *Journal of Metamorphic Geology, 16*(1), 142–146.

Lahfid, A., Beyssac, O., Deville, E., Negro, F., Chopin, C., & Goffé, B. (2010). Evolution of the Raman spectrum of carbonaceous material in low-grade metasediments of the Glarus Alps (Switzerland). *Terra Nova, 22*(5), 354-360.

Landry, K. R., Coutand, I., Whipp, D. M., Grujic, D., & Hourigan, J. K. (2016). Late Neogene tectonically driven crustal exhumation of the Sikkim Himalaya: Insights from inversion of multithermochronologic data. *Tectonics, 35*(3), 831-857.

Larson, K. P. (2018). Refining the structural framework of the Khimti Khola region, east-central Nepal Himalaya, using quartz textures and c-axis fabrics. *Journal of Structural Geology, 107*, 142-152.

Larson, K. P., & Godin, L. (2009). Kinematics of the Greater Himalayan sequence, Dhaulagiri Himal: implications for the structural framework of central Nepal. *Journal of the Geological Society, 166*(1), 25-43.

Law, R. D. (2014). Deformation thermometry based on quartz c-axis fabrics and recrystallization microstructures: A review. *Journal of structural Geology, 66*, 129-161.

Law, R., Searle, M., & Simpson, R. (2004). Strain, deformation temperatures and vorticity of flow at the top of the Greater Himalayan Slab, Everest Massif, Tibet. *Journal of the Geological Society, 161*(2), 305-320.

Law, R. D., Jessup, M. J., Searle, M. P., Francsis, M. K., Waters, D. J., & Cottle, J. M. (2011). Telescoping of isotherms beneath the South Tibetan Detachment System,

Mount Everest Massif. *Journal of Structural Geology, 33*(11), 1569-1594. http://linkinghub.elsevier.com/retrieve/pii/S0191814111001532
Le Fort, P. (1975). Himalayas: the collided range. Present knowledge of the continental arc. *American Journal of Science, 275-A*, 1-44.
Liang, Y. (2017). Effect of pressure on closure temperature of a trace element in cooling petrological systems. *Contributions to Mineralogy and Petrology, 172*(2-3), 8.
Long, S., McQuarrie, N., Tobgay, T., & Grujic, D. (2011a). Geometry and crustal shortening of the Himalayan fold-thrust belt, eastern and central Bhutan. *Geological Society of America Bulletin, 123*(7-8), 1427-1447.
Long, S., McQuarrie, N., Tobgay, T., Grujic, D., & Hollister, L. (2011b). Geologic map of Bhutan. *Journal of Maps, 7*(1), 184-192.
Long, S., McQuarrie, N., Tobgay, T., & Hawthorne, J. (2011c). Quantifying internal strain and deformation temperature in the eastern Himalaya, Bhutan: Implications for the evolution of strain in thrust sheets. *Journal of Structural Geology, 33*(4), 579-608. http://dx.doi.org/10.1016/j.jsg.2010.12.011
Long, S., McQuarrie, N., Tobgay, T., Rose, C., Gehrels, G., & Grujic, D. (2011d). Tectonostratigraphy of the Lesser Himalaya of Bhutan: Implications for the along-strike stratigraphic continuity of the northern Indian margin. *Geological Society of America Bulletin, 123*(7-8), 1406-1426.
Long, S. P., Gordon, S. M., Young, J. P., & Soignard, E. (2016). Temperature and strain gradients through Lesser Himalayan rocks and across the Main Central thrust, south central Bhutan: Implications for transport-parallel stretching and inverted metamorphism. *Tectonics, 35*(8), 1863-1891.
Long, S. P., McQuarrie, N., Tobgay, T., Coutand, I., Cooper, F. J., Reiners, P. W., et al. (2012). Variable shortening rates in the eastern Himalayan thrust belt, Bhutan: Insights from multiple thermochronologic and geochronologic data sets tied to kinematic reconstructions. *Tectonics, 31*(5), n/a-n/a.
Kelley, S. (2002). Excess argon in K–Ar and Ar–Ar geochronology. Chemical Geology, 188(1-2), pp.1-22.
Marechal, A., Mazzotti, S., Cattin, R., Cazes, G., Vernant, P., Drukpa, D., et al. (2016). Evidence of interseismic coupling variations along the Bhutan Himalayan arc from new GPS data. *Geophysical Research Letters, 43*(24), 12399-12406.
Martin, A.J. (2017). A review of Himalayan stratigraphy, magmatism, and structure. *Gondwana Research, 49*, 42-80.
Mathew, G., De Sarkar, S., Pande, K., Dutta, S., Ali, S., Rai, A., & Netrawali, S. (2013). Thermal metamorphism of the Arunachal Himalaya, India: Raman thermometry and thermochronological constraints on the tectono-thermal evolution. *International Journal of Earth Sciences, 102*(7), 1911-1936.
Mazzotti, S., & Gueydan, F. (2018). Control of tectonic inheritance on continental intraplate strain rate and seismicity. *Tectonophysics, 746*, 602-610.
McKenzie, D., Jackson, J., & Priestley, K. (2005). Thermal structure of oceanic and continental lithosphere. *Earth and Planetary Science Letters, 233*(3-4), 337-349.
McQuarrie, N., & Ehlers, T. (2015). Influence of thrust belt geometry and shortening rate on thermochronometer cooling ages: Insights from thermokinematic and erosion modeling of the Bhutan Himalaya. *Tectonics, 34*(6), 1055-1079.
McQuarrie, N., & Ehlers, T. A. (2017). Techniques for understanding fold-and-thrust belt kinematics and thermal evolution. Linkages and Feedbacks in Orogenic Systems, GSA Memoirs, edited by: Law, RD, Thigpen, JR, Merschat, AJ, and Stowell, HH, 213, 25-54.

McQuarrie, N., Robinson, D., Long, S., Tobgay, T., Grujic, D., Gehrels, G., & Ducea, M. (2008). Preliminary stratigraphic and structural architecture of Bhutan: Implications for the along strike architecture of the Himalayan system. *Earth and Planetary Science Letters, 272*(1-2), 105-117.

McQuarrie, N., Tobgay, T., Long, S. P., Reiners, P. W., & Cosca, M. A. (2014). Variable exhumation rates and variable displacement rates: Documenting recent slowing of Himalayan shortening in western Bhutan. *Earth and Planetary Science Letters, 386*, 161-174.

McQuarrie, N., Eizenhöfer, P.R., Long, S.P., Tobgay, T., Ehlers, T.A., Blythe, A., Morgan, L., Gilmore, M. and Dering, G. (2019). The influence of foreland structures on hinterland cooling: evaluating the drivers of exhumation in the eastern Bhutan Himalaya. *Tectonics*. https://doi.org/10.1029/2018TC005340

Morgan, D., Jollands, M., Lloyd, G., & Banks, D. (2014). Using titanium-in-quartz geothermometry and geospeedometry to recover temperatures in the aureole of the Ballachulish Igneous Complex, NW Scotland. *Geological Society, London, Special Publications, 394*(1), 145-165.

Morgan, S. S., & Law, R. D. (2004). Unusual transition in quartzite dislocation creep regimes and crystal slip systems in the aureole of the Eureka Valley–Joshua Flat–Beer Creek pluton, California: a case for anhydrous conditions created by decarbonation reactions. *Tectonophysics, 384*(1-4), 209-231.

Mottram, C. M., Argles, T., Harris, N., Parrish, R., Horstwood, M., Warren, C., & Gupta, S. (2014a). Tectonic interleaving along the Main Central Thrust, Sikkim Himalaya. *Journal of the Geological Society, 171*(2), 255-268.

Mottram, C. M., Parrish, R. R., Regis, D., Warren, C. J., Argles, T. W., Harris, N. B., & Roberts, N. M. (2015). Using U-Th-Pb petrochronology to determine rates of ductile thrusting: Time windows into the Main Central Thrust, Sikkim Himalaya. *Tectonics, 34*(7), 1355-1374.

Mottram, C. M., Warren, C. J., Regis, D., Roberts, N. M., Harris, N. B., Argles, T. W., & Parrish, R. R. (2014). Developing an inverted Barrovian sequence; insights from monazite petrochronology. *Earth and Planetary Science Letters, 403*, 418-431.

Mottram, C.M., Warren, C.J., Halton, A.M., Kelley, S.P. and Harris, N.B. (2015). Argon behaviour in an inverted Barrovian sequence, Sikkim Himalaya: the consequences of temperature and timescale on 40Ar/39Ar mica geochronology. Lithos, 238, pp.37-51.

Mulch, A., & Cosca, M. A. (2004). Recrystallization or cooling ages: in situ UV-laser 40Ar/39Ar geochronology of muscovite in mylonitic rocks. *Journal of the Geological Society, 161*(4), 573-582.

Mulch, A., Cosca, M.A., Andresen, A. and Fiebig, J. (2005). Time scales of deformation and exhumation in extensional detachment systems determined by high-spatial resolution in situ UV-laser 40Ar/39Ar dating. Earth and Planetary Science Letters, 233(3-4), pp.375-390.

Nachlas, W. O., Whitney, D. L., Teyssier, C., Bagley, B., & Mulch, A. (2014). Titanium concentration in quartz as a record of multiple deformation mechanisms in an extensional shear zone. *Geochemistry, Geophysics, Geosystems, 15*(4), 1374-1397.

Nachlas, W. O., and G. Hirth (2015), Experimental constraints on the role of dynamic recrystallization on resetting the Ti-in-quartz thermobarometer, J. Geophys. Res. Solid Earth, 120, 8120–8137, doi:10.1002/2015JB012274.

Naito, N., Ageta, Y., Iwata, S., Matsuda, Y., & Suzuki, R. (2006). Glacier shrinkages and climate conditions around Jichu Dramo Glacier in the Bhutan Himalayas from 1998 to 2003. *Bulletin of glaciological research, 23*, 51-61.

Negrini, M., Stünitz, H., Berger, A., & Morales, L. F. (2014). The effect of deformation on the TitaniQ geothermobarometer: an experimental study. *Contributions to Mineralogy and Petrology, 167*(3), 1-22.

Negro, F., Beyssac, O., Goffé, B., Saddiqi, O., & Bouybaouene, M. (2006). Thermal structure of the Alboran Domain in the Rif (northern Morocco) and the Western Betics (southern Spain). Constraints from Raman spectroscopy of carbonaceous material. *Journal of Metamorphic Geology, 24*(4), 309.

Nelson, K.D., Zhao, W., Brown, L.D., Kuo, J., Jinkai Che, J., Xianwen Liu, X., Klemperer, S.L., Makovsky, Y., Meissner, R., Mechie, J., Kind, R., Wenzel, F., Ni, J., Nabelek, J., Chen, L., Tan, H., Wei, W., Jones, A.G., Booker, J., Unsworth, M., Kidd, W.S.F., Hauck, M., Alsdorf, D., Ross, A., Cogan, M., Wu, C., Sandvol, E., and Edwards, M., (1996). Partially molten middle crust beneath southern Tibet; synthesis of Project IN- DEPTH results, *Science* 274, 1684-1688. doi: 10.1126/science.274.5293.1684.

Ostapenko, G., Gamarnik, M. Y., Gorogotskaya, L., Kuznetsov, G., Tarashchan, A., & Timoshkova, L. (1987). Isomorphism of titanium substitution for silicon in quartz: experimental data. *Mineral Zh, 9*, 30-40.

Ostapenko, G., Tarashchan, A., & Mitsyuk, B. (2007). Rutile-quartz geothermobarometer. *Geochemistry International, 45*(5), 506-508.

Parui, C., & Bhattacharyya, K. (2018). Duplex and along-strike structural variation: A case study from Sikkim Himalayan fold thrust belt. *Journal of Structural Geology, 113*, 62-75.

Parsons, A. J., R. D. Law, G. E. Lloyd, R. J. Phillips, and M. P. Searle (2016a), Thermo-kinematic evolution of the Annapurna-Dhaulagiri Himalaya, central Nepal: The Composite Orogenic System, *Geochem. Geophys. Geosyst.*, **17**, 1511–1539, doi:10.1002/2015GC006184.

Peternell, M., Hasalová, P., Wilson, C. J., Piazolo, S., & Schulmann, K. (2010). Evaluating quartz crystallographic preferred orientations and the role of deformation partitioning using EBSD and fabric analyser techniques. *Journal of Structural Geology, 32*(6), 803-817.

Press, W. H., Flannery, B. P., Teukolsky, S. A., & Vetterling, W. T. (1992). *Numerical recipes in FORTRAN: The art of scientific computing* (2nd ed.). Cambridge, England: Cambridge University Press.

Priestley, K., Jackson, J., & McKenzie, D. (2008). Lithospheric structure and deep earthquakes beneath India, the Himalaya and southern Tibet. *Geophysical Journal International, 172*(1), 345-362.

Rahl, J., Anderson, K., Brandon, M., & Fassoulas, C. (2005). Raman spectroscopic carbonaceous material thermometry of low-grade metamorphic rocks: calibration and application to tectonic exhumation in Crete, Greece. *Earth and Planetary Science Letters, 240*(2), 339-354.

Ramseyer, K., Baumann, J., Matter, A., & Mullis, J. (1988). Cathodoluminescence colours of a-quartz. *Mineralogical Magazine, 52*(368), 669-677.

Rantitsch, G., Sachsenhofer, R., Hasenhüttl, C., Russegger, B., & Rainer, T. (2005). Thermal evolution of an extensional detachment as constrained by organic metamorphic data and thermal modeling: Graz Paleozoic Nappe Complex (Eastern Alps). *Tectonophysics, 411*(1-4), 57-72.

Ray, S. K., Bandyopadhyay, B. K., & Razdan, R. K. (1989). Tectonics of a part of the Shumar allochthon in eastern Bhutan. *Tectonophysics, 169*, 51-58.

Regis, D., Warren, C. J., Young, D., & Roberts, N. (2014). Tectono-metamorphic evolution of the Jomolhari massif: Variations in timing of syn-collisional metamorphism across western Bhutan. *Lithos, 190–191*, 449–466.

Rickwood, P., & Sambridge, M. (2006). Efficient parallel inversion using the Neighbourhood Algorithm. *Geochemistry Geophysics Geosystems, 7*(11).
Sambridge, M. (1999a). Geophysical inversion with a neighbourhood algorithm -I. Searching a parameter space. *Geophysical Journal International, 138,*, 479-494.
Sambridge, M. (1999b). Geophysical inversion with a neighbourhood algorithm—II. Appraising the ensemble. *Geophysical Journal International, 138*(3), 727-746.
Schmid, S. M. (1994). Textures of geological materials: computer model predictions versus empirical interpretations based on rock deformation experiments and field studies. In H. J. Bunge, S. Siegesmund, W. Skrotzki, & K. Weber (Eds.), *Textures of Geological Materials* (pp. 279-302). Oberursel: DGM Informationsgesellschaft, Oberursel.
Schmid, S. M., Zingg, A., & Handy, M. R. (1987). The kinematics of movements along the Insubric Line and the emplacement of the Ivrea Zone. *Tectonophysics, 135*, 47-66.
Searle, M. P., Law, R. D., Godin, L., Larson, K. P., Streule, M. J., Cottle, J. M., & Jessup, M. J. (2008). Defining the Himalayan main central thrust in Nepal. *Journal of the Geological Society, 165*(2), 523-534.
Shrestha, S. B., Shrestha, J. N., & Sharma, S. R. (1987a). Geological map of far western Nepal, scale 1:250,000. *Topogr. Surv. Branch, Surv. Dep., Kathmandu*.
Shrestha, S. B., Shrestha, J. N., & Sharma, S. R. (1987b). Geological map of mid western Nepal, scale 1:250,000. *Topogr. Surv. Branch, Surv. Dep., Kathmandu*.
Singer, J., Obermann, A., Kissling, E., Fang, H., Hetényi, G. and Grujic, D. (2017). Along-strike variations in the Himalayan orogenic wedge structure in Bhutan from ambient seismic noise tomography. *Geochemistry, Geophysics, Geosystems, 18*(4), 1483-1498. https://doi.org/10.1002/2016GC006742
Spear, F. S., & Wark, D. A. (2009). Cathodoluminescence imaging and titanium thermometry in metamorphic quartz. *Journal of Metamorphic Geology, 27*(3), 187-205. http://doi.wiley.com/10.1111/j.1525-1314.2009.00813.x
Srivastava, P., & Mitra, G. (1994). Thrust geometries and deep structure of the outer and lesser Himalaya, Kumaon and Garhwal (India): Implications for evolution of the Himalayan fold-and-thrust belt. *Tectonics, 13*(1), 89-109.
Starnes, J.K., Long, S.P., Gordon, S.M., Zhang, J. and Soignard, E. (2020). Using quartz fabric intensity parameters to delineate strain patterns across the Himalayan Main Central thrust. *Journal of Structural Geology, 131*, 103941. https://doi.org/10.1016/j.jsg.2019.103941
Stipp, M., Stünitz, H., Heilbronner, R., & Schmid, S. M. (2002). The eastern Tonale fault zone: a 'natural laboratory' for crystal plastic deformation of quartz over a temperature range from 250 to 700 ºC. *Journal of Structural Geology, 24*, 1861-1884.
Stüwe, K., & Foster, D. (2001). 40Ar/39Ar, pressure, temperature and fission track constraints on the age and nature of metamorphism around the main central thrust in the eastern Bhutan Himalaya. *Journal of Asian Earth Sciences, 19*(1-2), 85-95.
Swapp, S. M., & Hollister, L. S. (1991). Inverted metamorphism within the Tibetan slab of Bhutan: evidence for a tectonically transported heat source. *Canadian Mineralogist, 29*(4), 1019-1041.
Thomas, J., Watson, E. B., Spear, F., Shemella, P., Nayak, S., & Lanzirotti, A. (2010). TitaniQ under pressure: the effect of pressure and temperature on the solubility of Ti in quartz. *Contributions to Mineralogy and Petrology*, 1-17.
Thomas, J. B., Watson, E. B., Spear, F. S., & Wark, D. (2015). TitaniQ recrystallized: experimental confirmation of the original Ti-in-quartz calibrations. *Contributions to Mineralogy and Petrology, 169*(3), 1-16.

Tobgay, T., McQuarrie, N., Long, S., Kohn, M. J., & Corrie, S. L. (2012). The age and rate of displacement along the Main Central Thrust in the western Bhutan Himalaya. *Earth and Planetary Science Letters, 319*, 146-158.

Vannay, J.-C., Sharp, Z. D., & Grasemann, B. (1999). Himalayan inverted metamorphism constrained by oxygen isotope thermometry. *Contributions to Mineralogy and Petrology, 137*(1-2), 90-101.

Vermeesch, P. (2012). On the visualisation of detrital age distributions. *Chemical Geology, 312-313*, 190-194.

Vollmer, F. W. (2015). *Orient 3: a new integrated software program for orientation data analysis, kinematic analysis, spherical projections, and Schmidt plots.* Paper presented at the Geological Society of America, Abstracts with Programs.

Wark, D. A., Hildreth, W., Spear, F. S., Cherniak, D. J., & Watson, B. E. (2007). Pre-eruption recharge of the Bishop magma system. *Geology, 35*(3), 235-238; doi: 210.1130/G23316A.23311.

Wark, D. A., & Watson, E. B. (2006). TitaniQ: a titanium-in-quartz geothermometer. *Contributions to Mineralogy and Petrology, 152*, 743–754.

Warren, C. J., Grujic, D., Kellett, D. A., Cottle, J., Jamieson, R. A., & Ghalley, K. S. (2011). Probing the depths of the India-Asia collision: U-Th-Pb monazite chronology of granulites from NW Bhutan. *Tectonics, 30*(2), n/a-n/a.

Warren, C.J., Hanke, F. and Kelley, S.P.2012). When can muscovite 40Ar/39Ar dating constrain the timing of metamorphic exhumation?. Chemical Geology, 291, pp.79-86.

Warren, C. J., Singh, A. K., Roberts, N. M., Regis, D., Halton, A. M., & Singh, R. B. (2014). Timing and conditions of peak metamorphism and cooling across the Zimithang Thrust, Arunachal Pradesh, India. *Lithos, 200*, 94-110.

Waters, D. J. (2019). Metamorphic constraints on the tectonic evolution of the High Himalaya in Nepal: the art of the possible. *Geological Society, London, Special Publications, 483*, SP483-2018-2187.

Watt, G., Wright, P., Galloway, S., & McLean, C. (1997). Cathodoluminescence and trace element zoning in quartz phenocrysts and xenocrysts. *Geochimica et Cosmochimica Acta, 61*(20), 4337-4348.

Williams, J.R. and Platt, J.P. (2017) Superposed and refolded metamorphic isograds and superposed directions of shear during late orogenic extension in the Alborán Domain, southern Spain. *Tectonics*, *36*(5), pp.756-786.

Wilson, C. J., Russell-Head, D. S., Kunze, K., & Viola, G. (2007). The analysis of quartz c-axis fabrics using a modified optical microscope. *Journal of Microscopy, 227*(1), 30-41.

Yakymchuk, C., & Godin, L. (2012). Coupled role of deformation and metamorphism in the construction of inverted metamorphic sequences: an example from far-northwest Nepal. *Journal of Metamorphic Geology, 30*(5), 513-535.

Yin, A., Dubey, C. S., Kelty, T. K., Webb, A. A. G., Harrison, T. M., Chou, C. Y., & Célérier, J. (2010). Geologic correlation of the Himalayan orogen and Indian craton: Part 2. Structural geology, geochronology, and tectonic evolution of the Eastern Himalayan. *Geological Society of America Bulletin, 122*(3/4), 360-395.

Yu, H., Webb, A. A. G., & He, D. (2015). Extrusion vs. duplexing models of Himalayan mountain building 1: Discovery of the Pabbar thrust confirms duplex-dominated growth of the northwestern Indian Himalaya since Mid-Miocene. *Tectonics, 34*(2), 313-333.

**Table 1** Summary of temperatures obtained by RSCM. Full data are provided in Table S1 in the supporting information. For comparison only, temperatures calculated using the calibration by Rahl et al. (2005) are also reported. Temperatures are reported as standard means at the 1σ and 2 standard errors (2SE) confidence levels, accounting for both internal and external uncertainties.

**Table 1**

*Data and metamorphic temperature obtained by Raman Spectroscopy on Carbonaceous Material*

| Sample | Unit | *n* | *R1* Ratio (mean) | *R2* Ratio (mean) | *Beyssac temperature* | | | *Rahl Temperature* | | |
|---|---|---|---|---|---|---|---|---|---|---|
| | | | | | °C | 1$\sigma$ | 2SEM | °C | 1$\sigma$ | 2SEM |
| BH507 | Jaishidanda Fm. | 14 | 0.495 | 0.438 | 446.0 | 31.1 | 31.5 | 406.8 | 42 | 34.90 |
| BH511 | Baxa Group | 10 | 1.139 | 0.539 | 401.3 | 6.5 | 31.9 | 421.8 | 7 | 31.93 |
| BH513 | Daling Fm. | 11 | 0.582 | 0.419 | 454.4 | 9.6 | 30.7 | 448.9 | 13 | 31.15 |
| BH516 | Diuri Fm. | 10 | 1.758 | 0.634 | 358.7 | 2.1 | 31.7 | 373.7 | 3 | 31.68 |
| BH518 | Gondwana Fm. | 10 | 1.648 | 0.655 | 349.5 | 8.2 | 32.0 | 344.8 | 17 | 33.40 |
| BH519 | Gondwana Fm. | 10 | 1.543 | 0.635 | 358.5 | 10.4 | 32.3 | 357.9 | 20 | 34.06 |
| BH520 | Gondwana Fm. | 10 | 2.043 | 0.663 | 346.2 | 6.6 | 31.9 | 342.4 | 25 | 35.36 |
| BH521 | Gondwana Fm. | 11 | 2.012 | 0.683 | 337.0 | 7.0 | 30.4 | 322.4 | 20 | 32.47 |
| BH523 | Gondwana Fm. | 10 | 1.798 | 0.676 | 340.2 | 9.7 | 32.2 | 324.5 | 22 | 34.55 |
| BH524 | Baxa Group | 10 | 1.659 | 0.640 | 356.2 | 13.0 | 32.7 | 361.7 | 27 | 35.94 |
| BH525 | Daling Fm. | 11 | 0.565 | 0.414 | 456.8 | 22.2 | 33.0 | 449.7 | 29 | 34.86 |
| BH526A | Daling Fm. | 12 | 0.580 | 0.426 | 451.4 | 51.4 | 41.4 | 430.3 | 65 | 47.35 |
| BH526B | Daling Fm. | 12 | 0.401 | 0.355 | 483.1 | 11.5 | 29.6 | 473.9 | 17 | 30.49 |
| BH527 | Daling Fm. | 13 | 0.354 | 0.333 | 492.9 | 12.5 | 28.6 | 485.4 | 22 | 30.30 |
| BH528 | Daling Fm. | 11 | 0.288 | 0.309 | 503.4 | 13.2 | 31.2 | 492.6 | 23 | 33.19 |
| BH529 | Daling Fm. | 11 | 0.264 | 0.281 | 511.6 | 11.6 | 30.9 | 505.9 | 21 | 32.70 |
| BH909 | Jaishidanda Fm. | 24 | 0.320 | 0.254 | 528.1 | 23.4 | 22.5 | 559.8 | 23 | 22.54 |
| BH901 | Daling Fm. | 26 | 0.822 | 0.456 | 438.1 | 19.1 | 21.0 | 448.5 | 19 | 21.00 |
| BH904 | Daling Fm. | 18 | 0.774 | 0.485 | 444.9 | 20.3 | 21.9 | 399.1 | 20 | 25.44 |

Mean temperature is indicated with 1σ, the internal error (standard deviation of the temperature calculations) and the 2SEM which is the 2-standard error of the mean is calculated as the square root of the summed internal error and calibration error of ± 50 °C from the Beyssac et al. (2002) squared, divided by the square root of the number of analyses (n).

**Table 2** Summary of deformation temperatures obtained by Ti-in-quartz thermobarometry. The Ti-in-quartz data for all the analytical spots (Table S2 in the supporting information) within a sample were analyzed in the form of Kernel Density Estimator (KDE) following Vermeesch (2012) to constrain the two composition components of the entire data population within a sample.

**Table 2** Data and deformation temperatures obtained by Ti-in-quartz geothermobarometry

| Sample | Structural distance | Ti core (average) | | Ti rim (average) | | *T* core (°C) | | | *T* rim (°C) | | | |
|---|---|---|---|---|---|---|---|---|---|---|---|---|
| | m | ppm | mol | ppm | mol | *a* =1 P=9 kbar | *a*=0.4 P=9 kbar | ± 2SEM | *a*=1 P=9 kbar | *a*=1 P=4 kbar | *a*=0.4 P=4 kbar | ± 2SEM |
| BH 133 | -10.0 | 2.82 | 3.54E-06 | 2.23 | 2.80E-06 | 450.5 | 506.6 | 3.2 | 437.4 | 356.7 | 356.7 | 9.8 |
| BH 804 | -265.3 | 3.93 | 4.94E-06 | 3.41 | 4.29E-06 | 469.9 | 529.2 | 2.9 | 461.6 | 378.1 | 378.1 | 7.6 |
| BH 132 | -1400.0 | 1.68 | 2.11E-06 | 1.21 | 1.52E-06 | 422.2 | 473.8 | 10.2 | 405.5 | 328.4 | 328.4 | 10.6 |
| BH 806 | -1511.9 | 2.70 | 3.39E-06 | 2.41 | 3.03E-06 | 448.1 | 503.8 | 2.7 | 441.7 | 360.5 | 360.5 | 8.4 |
| BH 57 | -2403.9 | 1.56 | 1.96E-06 | 1.04 | 1.31E-06 | 418.5 | 469.5 | 7.2 | 398.1 | 321.9 | 321.9 | 4.5 |
| BH 56 | -2551.7 | 1.47 | 1.84E-06 | 1.16 | 1.45E-06 | 415.2 | 465.7 | 3.2 | 403.2 | 326.3 | 326.3 | 6.5 |
| BH 809 | -2551.7 | 3.21 | 4.03E-06 | 3.21 | 4.03E-06 | 457.9 | 515.3 | 6.7 | 445.4 | 363.7 | 363.7 | 16.5 |
| BH 810 | -2757.4 | 2.33 | 2.82E-06 | 2.33 | 2.82E-06 | 432.3 | 485.5 | 5.3 | 432.3 | 352.1 | 352.1 | 10.2 |
| BH 812 | -3098.0 | 1.02 | 1.29E-06 | 0.88 | 1.10E-06 | 397.2 | 445.1 | 3.1 | 389.8 | 314.5 | 314.5 | 4.8 |

gray fields are the values adopted in this manuscript

*a* indicates $a_{TiO2}$

2SEM is the 2-standard error of the mean calculated as the square root of the summed squared 2$\sigma$ accuracy of the Ti-in-Quartz thermometer in the temperature range between 700 and 400 °C of ± 4–5 °C (Wark and Watson, 2006), the analytical precision of the geothermometer using the SHRIMP-RG analyses of ±1–3 °C (Grujic et al., 2011), and the standard deviation of the measurements, divided by the square root of the number of analyses (n, Table S2). It does not include the uncertainty on *a* and P.

**Table 3** Deformation thermometry based on quartz c-axis fabrics

**Table 3** Deformation thermometry based on quartz c-axis fabrics

| Sample | Latitude (°N) | Longitude (°E) | Structural distance beneath the MCT [m] | Opening angle (average) | T (°C) | error ( ± °C) | pressure [kbar] | TP (°C)TP (°C) | error ( ± °C) |
|---|---|---|---|---|---|---|---|---|---|
| BH 801 | 91.480770 | 27.299400 | 0 | 75 | 556.0 | 50 | 3.3 | 547.0 | 60 |
| BH 803 | 91.480770 | 27.299400 | -20 | 71 | 538.0 | 50 | 3.3 | 524.5 | 60 |
| BH 39 | 27.284253 | 91.446337 | -265 | 67 | 510.0 | 50 | 3.2 | 499.3 | 60 |
| **BH 39** | 27.284253 | 91.446337 | -265 | 68 | 518.0 | 50 | 3.2 | 505.4 | 60 |
| BH 58 | 27.295139 | 91.457000 | -1333 | 72 | 597.0 | 50 | 3.3 | 530.2 | 60 |
| BH 58R | 27.295139 | 91.457000 | -1333 | 80 | 600.0 | 50 | 3.5 | 576.3 | 60 |
| BH 806 | 27.295260 | 91.453540 | -1512 | 59 | 455.0 | 50 | 2.9 | 442.8 | 60 |
| BH 807 | 91.455560 | 27.286290 | -1736 | 60 | 462.0 | 50 | 2.9 | 449.7 | 60 |
| **BH 18** | 27.284877 | 91.447472 | -2000 | 62 | 475.8 | 50 | 2.9 | 463.2 | 60 |
| BH 808 | 91.444660 | 27.281840 | -2456 | 80 | 600.0 | 50 | 3.5 | 576.3 | 60 |
| BH 809 | 27.281650 | 91.433520 | -2552 | 65 | 497.0 | 50 | 3.1 | 485.4 | 60 |
| BH 810 | 27.273950 | 91.424490 | -2757 | 63 | 483.0 | 50 | 3.0 | 471.2 | 60 |
| BH 17 | 27.270754 | 91.418918 | -2800 | 60 | 462.0 | 50 | 2.9 | 449.7 | 60 |
| **BH 17** | 27.270754 | 91.418918 | -2800 | 56 | 434.4 | 50 | 2.9 | 421.4 | 60 |

| | | | | | | | | | |
|---|---|---|---|---|---|---|---|---|---|
| BH 812 | 27.256560 | 91.410180 | -3098 | 52 | 407.0 | 50 | 2.6 | 386.7 | 60 |
| **BH 12** | 27.309817 | 91.156767 | -3098 | 49 | 386.1 | 50 | 2.6 | 362.3 | 60 |

On samples in bold the opening angles of the quartz c-axis fabrics were measuered on the diagrams publsihed by Grujic et al. (1996).

**Table 4** Summary of muscovite $^{40}Ar/^{39}Ar$ results. All the data are provided in Table S5 and at the Geochron database (http://www.geochron.org).

| Sample | Latitude °N | Longitude °E | Elevation (m) | Tectonic unit | Age (Ma) | ± 1 σ (Ma) | Age type | closure type |
|---|---|---|---|---|---|---|---|---|
| BH 54 | 27.241834 | 91.527189 | 2580 | Jaishidanda fm | 15.56 | 0.60 | isochron | cooling |
| BH 801 | 27.2994 | 91.48077 | 735 | Jaishidanda fm | 11.76 | 0.17 | plateau | reset |
| BH 802g | 27.2994 | 91.48077 | 735 | Jaishidanda fm | 11.70 | 0.97 | isochron | reset |
| BH 802m | 27.2994 | 91.48077 | 735 | Jaishidanda fm | 11.10 | 0.85 | isochron | reset |
| BH 805 | 27.29865 | 91.47592 | 763 | LHS - gneiss | 12.18 | 0.17 | plateau | reset |

Table 5. Pecube model parameters

| Parameter name | Parameter range | Units | Parameter Symbol | Reference |
|---|---|---|---|---|
| ***Material Properties*** | | | | |
| Thermal diffusivity | 35 | $km^2/Ma$ | $\alpha$ | |
| Radiogenic heat production | 1.6 | $\mu W/m^3$ | A | |
| ***Pecube Model Parameters*** | | | | |
| Mean annual surface temperature in the foreland | 25 | °C | $T_s$ | |
| Atmospheric lapse rate | 6 | °C/km | L | Naito et al, 2006 |
| Basal Temperature | **500-700** | °C | $T_b$ | |
| India-Eurasia convergence rate | 17 | mm/yr | $\nu_{conv}$ | Marechal et al., 2016 |
| Convergence partitioning | **Variable** | n/a | $\lambda$ | |
| Model time step | Optimal | years | | |
| Horizontal node spacing | 0.9 | km | | |
| Vertical node spacing (0-5km) | 0.9 | km | | |
| Vertical node spacing (5-15km) | 2.7 | km | | |
| Vertical node spacing (15-50km) | 8.1 | km | | |
| Model domain | 165x220x50 | km | | |
| Fault geometry | **Variable** | km | $(X_n, Z_n)$ | Singer et al., 2017, Hirschmiller et al., 2014; Coutand et al., 2014 and refs therein |
| Crustal accretion (south boundary) | **Variable** | km | $CA_{dist}$ | |
| Crustal accretion (north boundary) | **Variable** | km | $CA_{prox}$ | |
| Crustal accretion vertical rate | **Variable** | mm/yr | $\nu_{CA}$ | |

The bold entries indicate the free parameters that were inverted for in our numerical simulation

Table 6. Inversion results

| **Inversion name** | **RAB01** | **References** |
|---|---|---|
| Number of models | 21624 | |
| Best misfit | 0.45 | |
| Tb (°C) | **556** (500:700) | |
| ($X_8$, $Z_8$) (km) | (177;35:40) (177;**39.5**) | Coutand et al., 2014 |
| ($X_7$, $Z_7$) (km) | (120:140;20:35) (**120**;**33**) | |
| ($X_6$, $Z_6$) (km) | (90;20:25) (90;**20**) | Coutand et el., 2014 |
| ($X_5$, $Z_5$) (km) | (68;19.5) | Singer et al., 2017 |
| ($X_4$, $Z_4$) (km) | (58;12.5) | Singer et al., 2017 |
| ($X_3$, $Z_3$) (km) | (21;10) | Singer et al., 2017 |
| ($X_2$, $Z_2$) (km) | (7;4) | Hirschmiller et al., 2014 |
| ($X_1$, $E_1$) (km) | (0;0.5) | |
| Running time (Ma) | 15-0 | |
| Stage 1 (15-11 Ma) Partitioning factor ($\lambda_1$) | 0.25 | |
| Stage 2 (11-4.4 Ma) Partitioning factor ($\lambda_2$) | **0.7** (0.5:0.9) | |
| Stage 2 (4.4-0 Ma) Partitioning factor ($\lambda_3$) | **0.9** (0.5:0.9) | |
| Transition time *x* (Ma) | **4.4** (4:7) | |
| Vertical accretion rate ($V_{CA}$) (mm/a) | **0.9** (0:3) | |
| Vertical accretion zone south limit ($CA_{dist}$) (km) | **59.9** (15:60) | |
| Vertical accretion zone north limit ($CA_{prox}$) (km) | **141.1** (60:150) | |

Values separated by colons indicate the investigated range of a free parameters and the lowest misfit values for each parameter are indicated in bold.

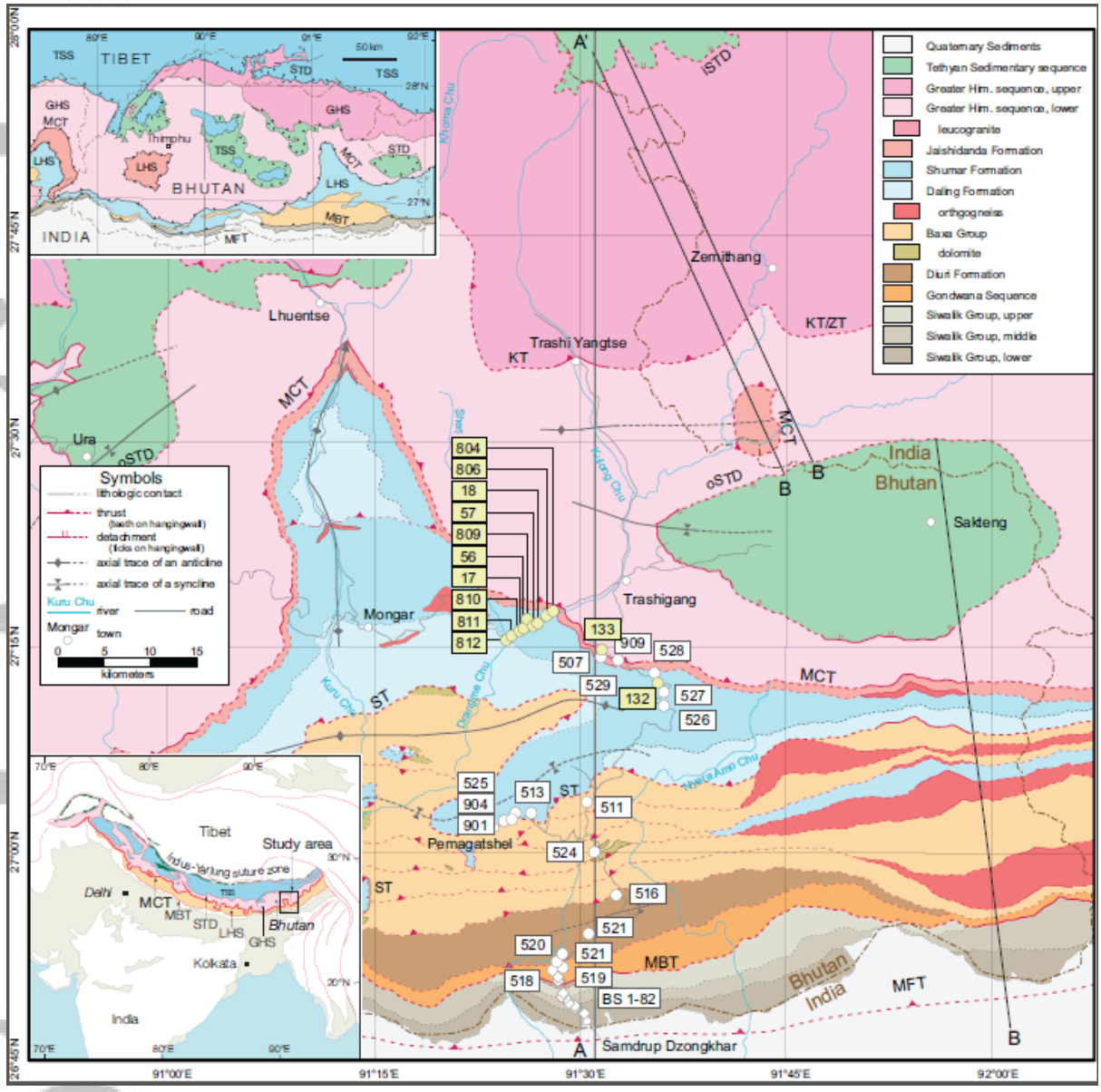


**Figure 1** Geological map of eastern Bhutan with thermometry sample locations. White boxes are the samples for RSCM, the yellow boxes are the samples for the Ti-in-quartz thermobarometry, and white lozenges are vitrinite reflectance data (Grujic et al., 2018). Geology after Long et al. (2011b) modified by data in McQuarrie et al. (2019), Grujic et al. (2018), and our observations. The cross section AA' in Figure 2 follows the latitude 90°32'E. B are lines of section by McQuarrie et al. (2019). Abbreviations are: MFT, Main Frontal Thrust; MBT, Main Boundary Thrust; ST, Shumar Thrust; MCT, Main Central Thrust; KT, Kakhtang Thrust; oSTD, Outer South Tibetan Detachment; iSTD, Inner South Tibetan Detachment. Insert in top left is the simplified geologic map of Bhutan and surroundings. Insert in lower left is the simplified tectonic map of the Himalaya and Tibet after Gansser (1983).

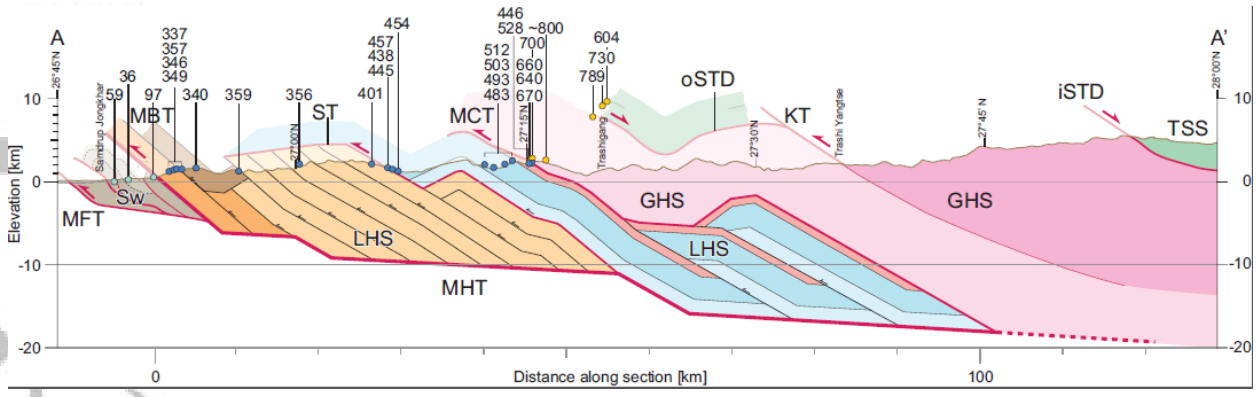


**Figure 2** Cross section AA' across the eastern Bhutan Himalaya. Temperatures (in °C) with blue circles were acquired by RSCM thermometry, and temperatures with yellow circles were acquired by traditional thermobarometry (Daniel et al., 2003; Kellett et al., 2010). Cross section after Long et al. (2011a), modified by data from Coutand et al. (2014) for the MHT geometry, Hirschmiller et al., (2010) for the geometry of the Sub-Himalaya, and our observations for the STD. The section across the LHS is therefore not retrodeformable as in the original form by Long et al. (2011a). Abbreviations are: MFT, Main Frontal Thrust; MBT, Main Boundary Thrust; ST, Shumar Thrust; MCT, Main Central Thrust; KT, Kakhtang Thrust; oSTD, Outer South Tibetan Detachment; iSTD, Inner South Tibetan Detachment.

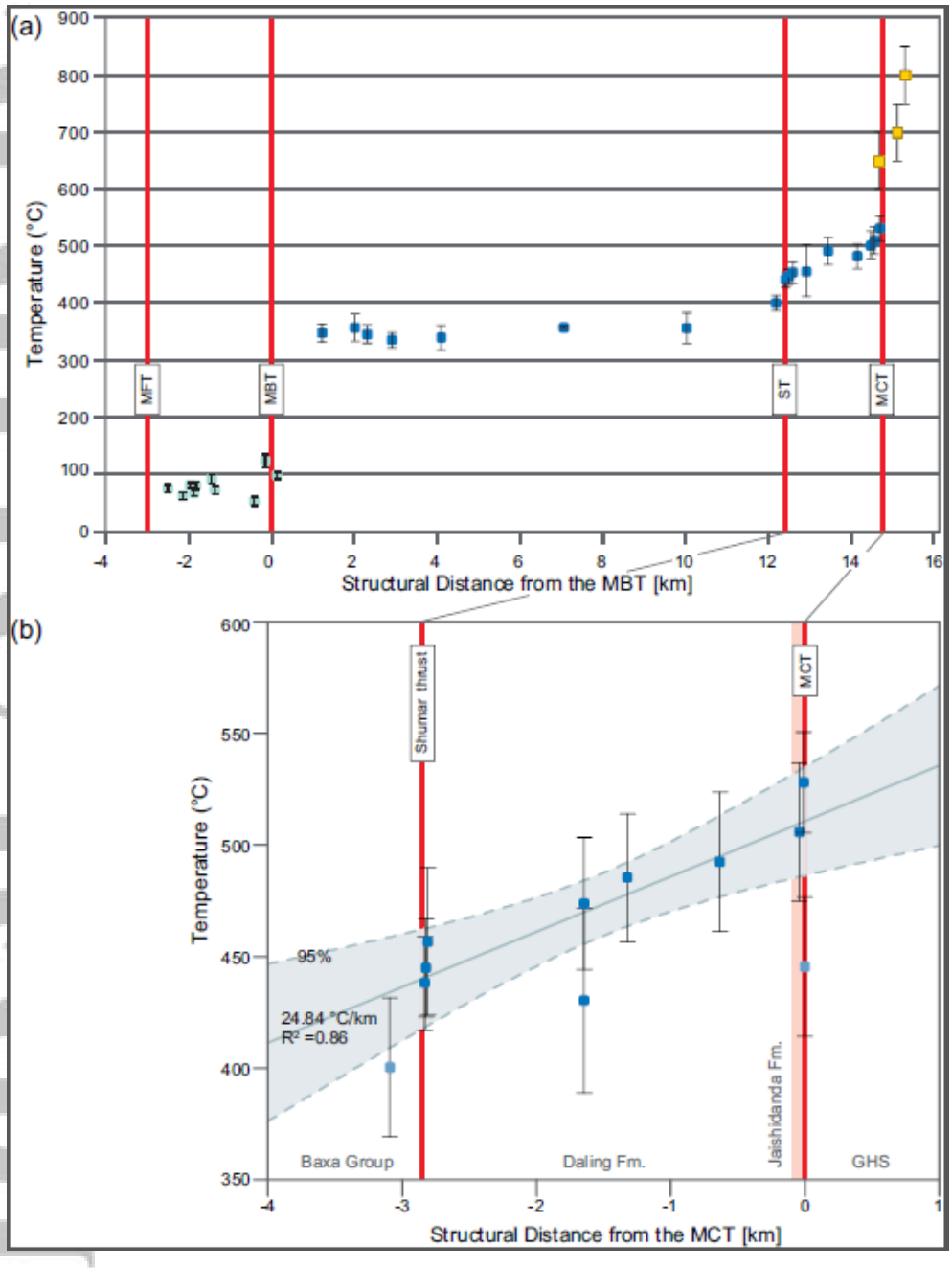


**Figure 3** Peak temperatures across the LHS of the eastern Bhutan Himalaya. (a) Temperatures obtained by RSCM (in blue) plotted with their structural distance from the MBT according to the cross section (Figure 2). Temperatures in green from the Siwaliks group sediments are vitrinite reflectance data (Grujic et al., 2018). Yellow: metamorphic peak temperatures in the Jaishidanda formation and at the base of the GHS in eastern Bhutan (Daniel et al., 2003). (b) RSCM temperatures in the internal duplex plotted with their structural distance from the MCT. RSCM data are reported with the 2 SEM (Table 1). All the structural distances from the main shear zones and faults were measured along the cross section of Long et al. (2011a).

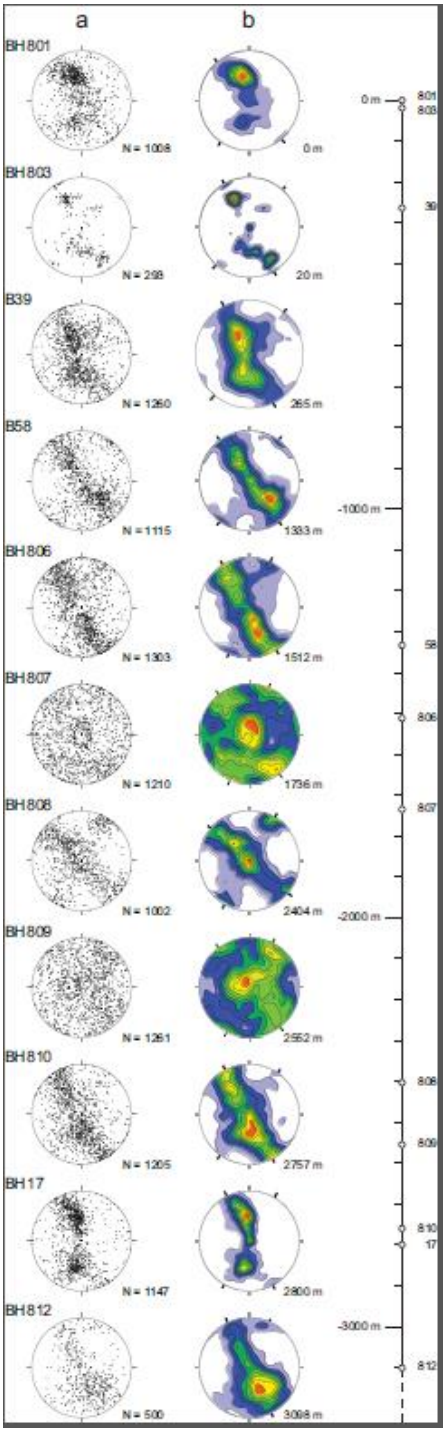


**Figure 4.** Microstructure. (a and b) Equal-area lower hemisphere stereonet projections of quartz *c*-axis measurements. All specimens are oriented such that north is to the right and south is to the left such that a 'sinistral' asymmetry corresponds to a top-to-the-south sense of shear. The foliation for each specimen plots as a vertical east-west plane while the maximum extension direction plots as a horizontal east-west line. (b) With the exception of BH808, each specimen is contoured as probability density with 10 steps as implemented in the software program Orient (Vollmer, 2015); BH808 is contoured using 20 steps. Warmer colors

indicate increased probability. (c) Micrographs of representative microstructures. Sample BH507 micaschist shows deformed white mica containing graphite inclusions. Sample BH801 shows mica blades deformed by top-to-the south sense shear bands. Sample BH 57 shows the microstructural evolution observed in all quartz mylonites. Larger grains were deformed by GBR recrystallisation The quartz microstructure, however, exhibits 120° triple junctions and straight or gently curved grain boundaries characteristic of foam or partial-foam microstructure. These grains are overprinted by SGR recrystallisation. Note the same size and orientation of subgrains in quartz porphyroclasts and of the new grains. Sample BH 812 is the structurally lowest. Note the progressive decrease of grain size from the highest (BH 801) to the lowest (BH812) consistent with the lower deformation temperatures. Scale bar on all micrograpahs is 1 mm.

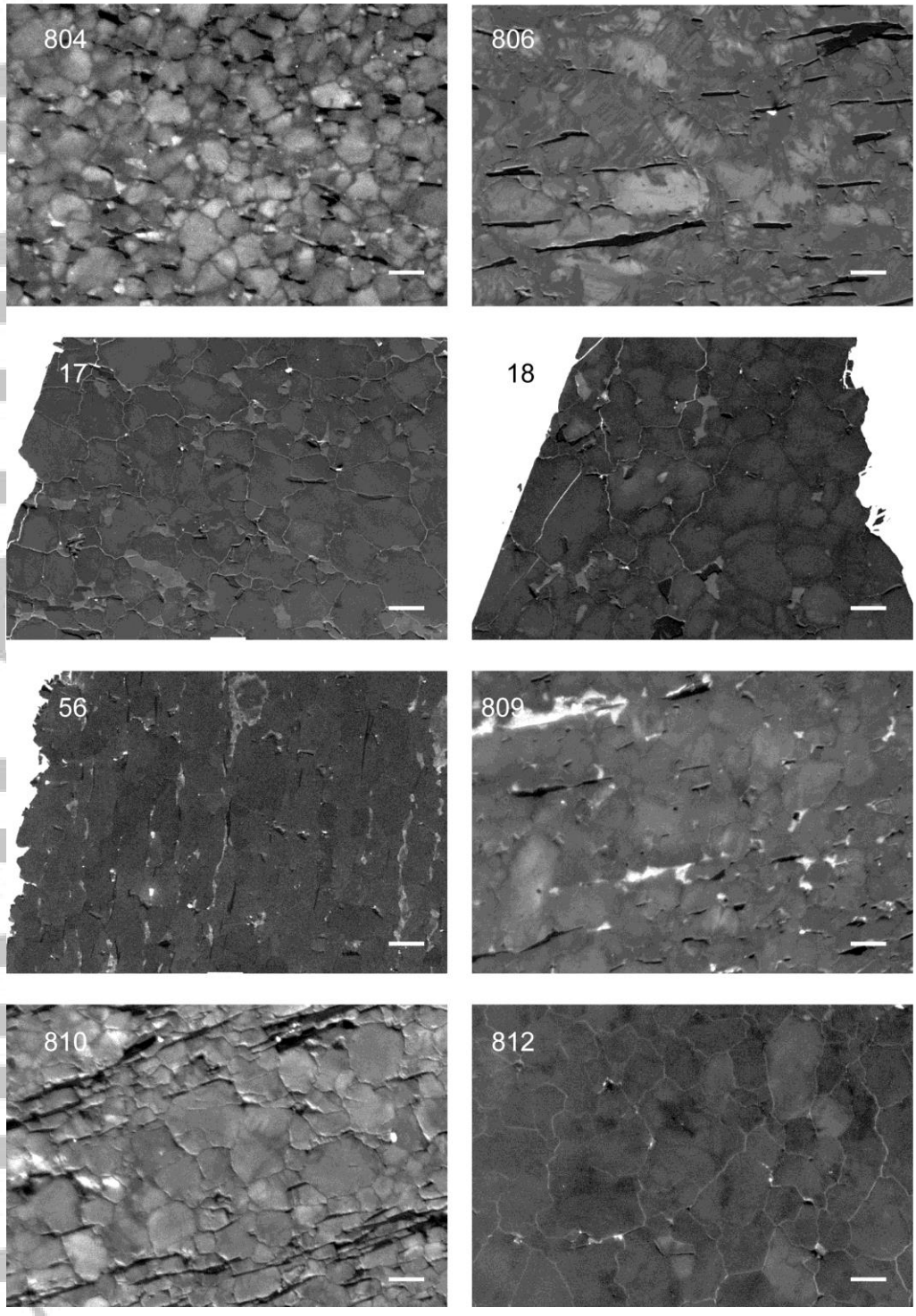


**Figure 5** Scanning electron microscope, cathodoluminescence (CL) patterns in the LHS quartzites showing brighter luminescent cores and darker rims for dynamically recrystallized grains.

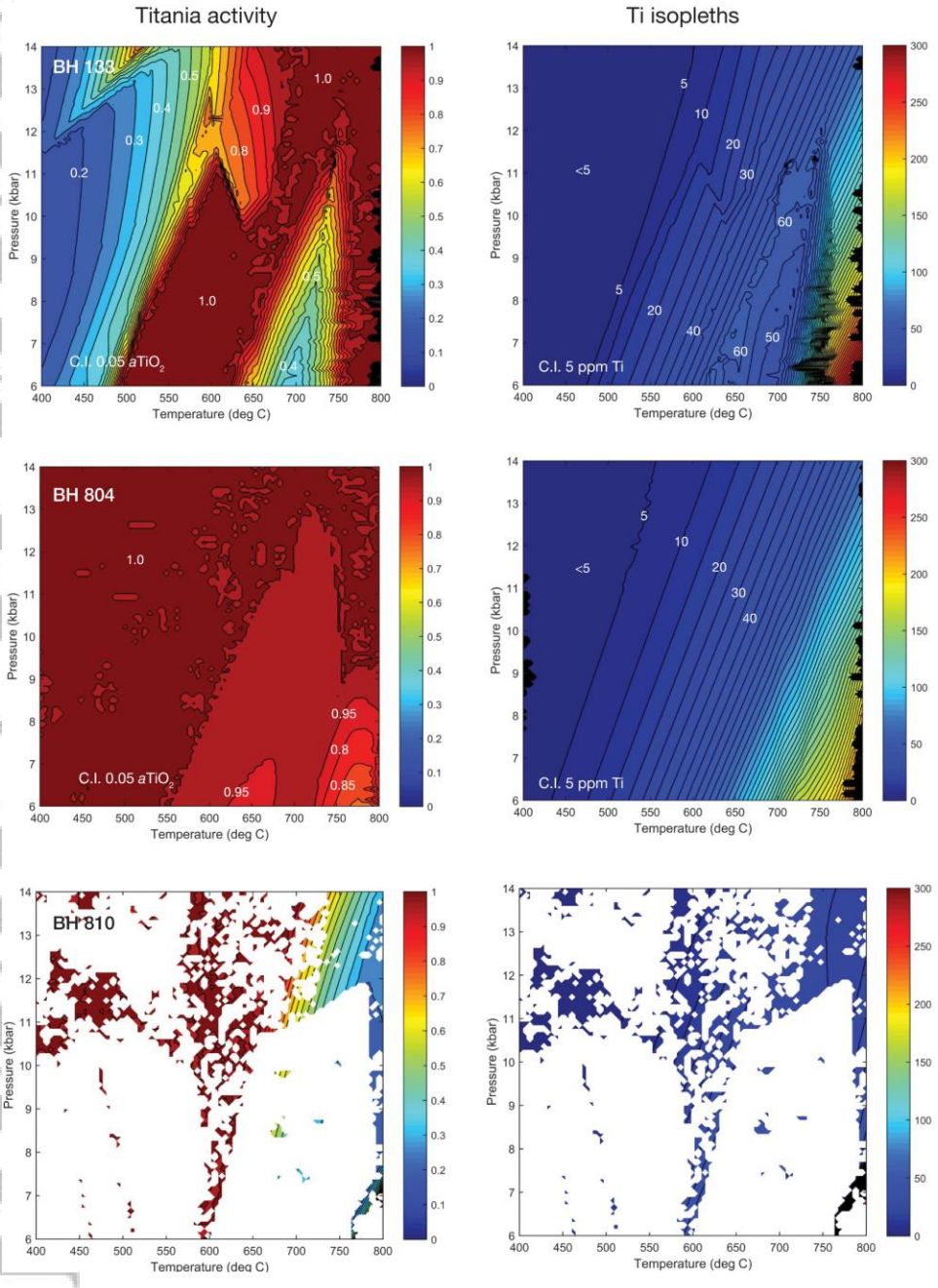


**Figure 6** Titania activities were calculated following the modeling approach of (Ashley & Law, 2015). Modeled $a_{TiO2}$ for bulk composition and Ti isopleth projection, based on the calculated activity map. (a) Sample (BH 133, (b) sample BH 801, (c) Sample BH 810. The $a_{TiO2}$ in a sample is estimated using the combination of Ti concentration in analytical spots and the independently estimated range of peak temperature and pressure. For samples with low bulk $TiO_2$ (<0.05 wt. %), no chemical potentials could be calculated for there is no stable Ti-bearing phases in abundance (results in "NaN" values in the output). X-ray fluorescence bulk rock data are given in the Table S3 and the solution models considered in thermodynamic calculations are given in table S4 as supporting information.

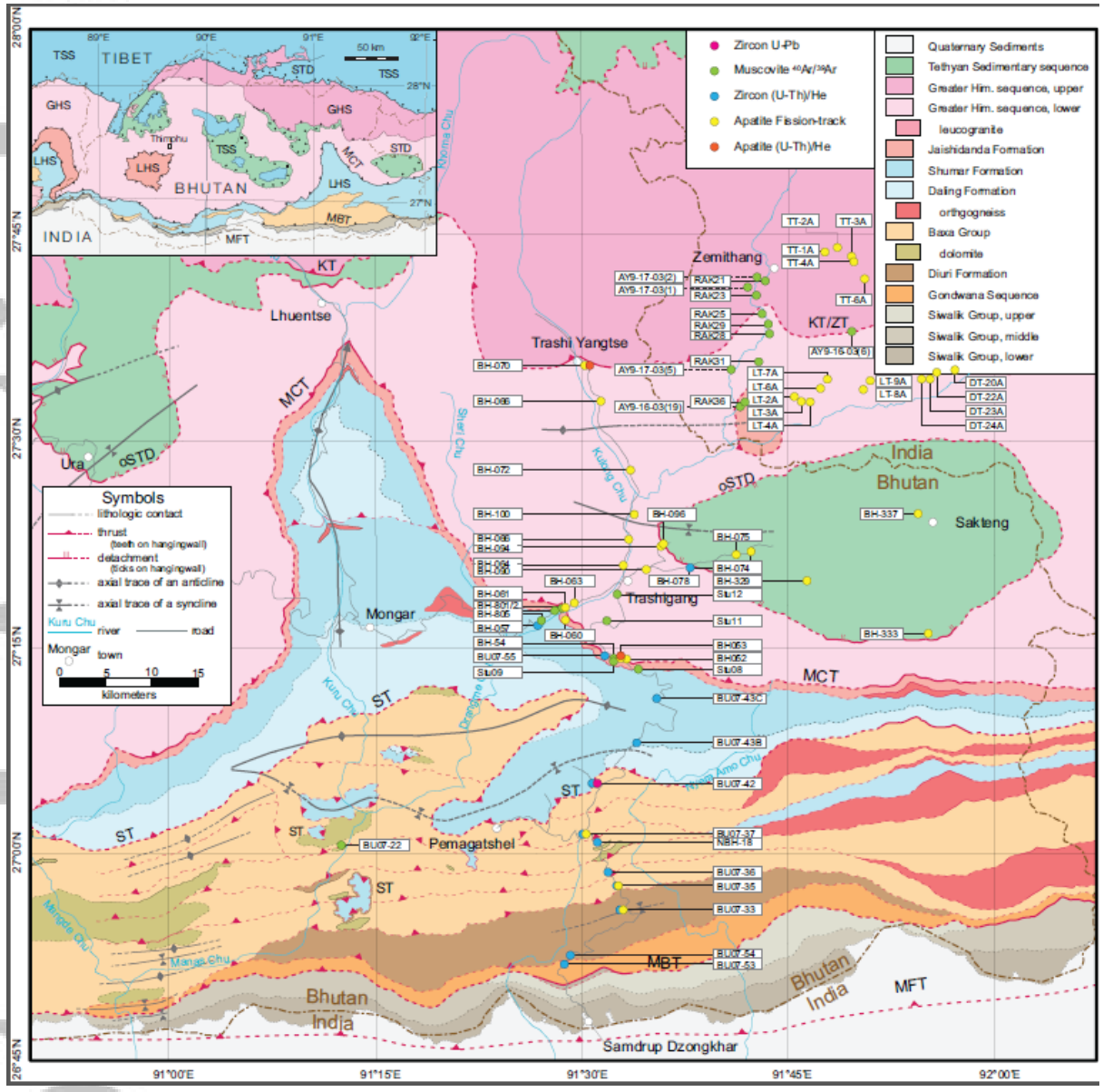


**Figure 7** Geological map of eastern Bhutan (same as Figure 1) showing the location of thermochronometric samples. Locations details and ages are listed in Table S6.

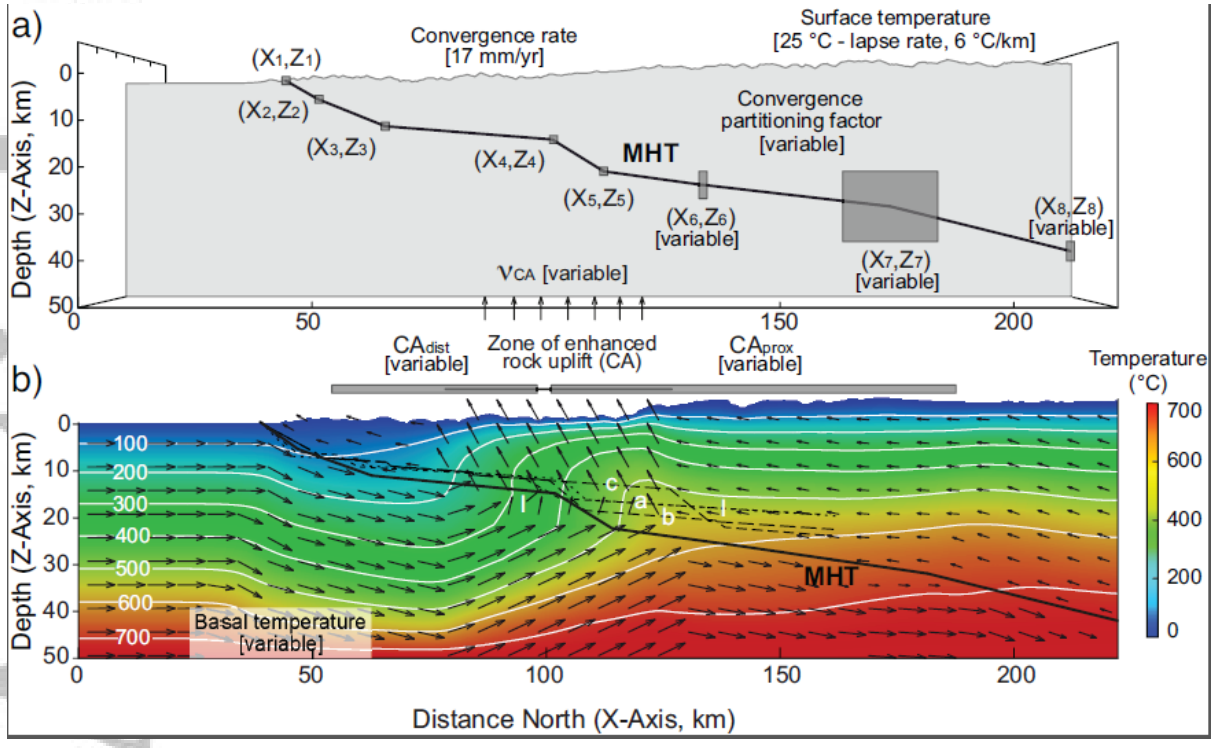


**Figure 8.** Thermo-kinematic model boundary conditions, free parameters (variables) and example thermal solution (parameters and variable ranges are given in Tables 5 and 6). Reported is the MHT geometry from our lowest misfit forward model. a) The kinematic model has Indo-Tibetan convergence partitioned on either side of the MHT, which is defined by a series of points along its length that may occupy any position within each corresponding search box. Point 1 ($X_1$, $Z_1$) is the modern surface trace of the MHT; Point 2 is from Hirschmiller et al. (2014), Points 3 to 5 from Singer et al. (2017), and points 6 and 8 from Coutand et al. (2014). ( b) Isotherms (thin white lines) show significant perturbations to the subsurface thermal field, mainly from advection through the velocity field (black arrows) generated by the kinematic model. Enhanced rock uplift simulates vertical crustal accretion (CA) at a rate $v_{ca}$ resulting from duplex development. Instantaneous exhumation rates correspond to the vertical component of the velocity vectors. Figure modified after Coutand et al. (2014) and Landry et al. (2016). For comparison indicated are the published MHT geometries in dashed lines: (l) Long et al. (2011) section AA' in figure 1. (a) McQuarrie et al. (2019) model a; (b) McQuarrie et al. (2019) model b; (c) McQuarrie et al. (2019) model c. Line of section by McQuarrie et al. (2019) is indicated as B in figure 1.

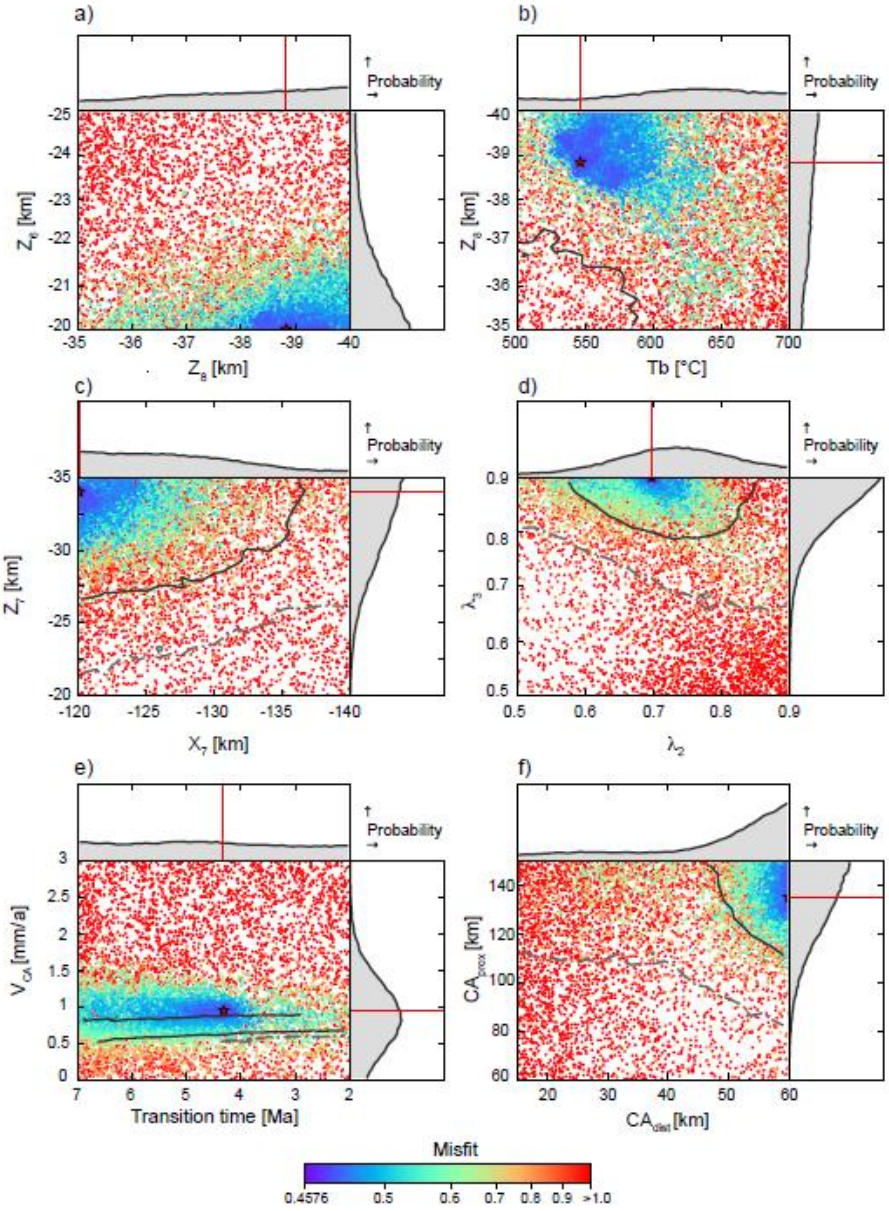


**Figure 9** Inversion results solving for 11 free parameters (see Table 5) with (a) $Z_6$ versus $Z_8$, (b) $Z_8$ versus Tb, (c) $Z_7$ versus $X_7$, (d) $\lambda_2$ versus $\lambda_3$, (e) $V_{CA}$ versus *Transition time*, and (f) $CA_{prox}$ versus $CA_{dist}$. Each dot represents a single forward model, and its color corresponds to the goodness of fit to the data (red (blue) dot = highest (lowest) misfit). The red star represents the parameter values obtained from the forward model with the lowest misfit. One-dimensional posterior probability density functions (1-D PPDFs) derived from the NA appraisal are shown adjacent to the axes for each parameter. The red lines indicate parameter values for the lowest misfit forward model. Two-dimensional PPDFs (2-D PPDFs) are represented by lines overlying the scatter diagram where the solid black line is the 1σ confidence interval and the dashed line the 2σ confidence interval.

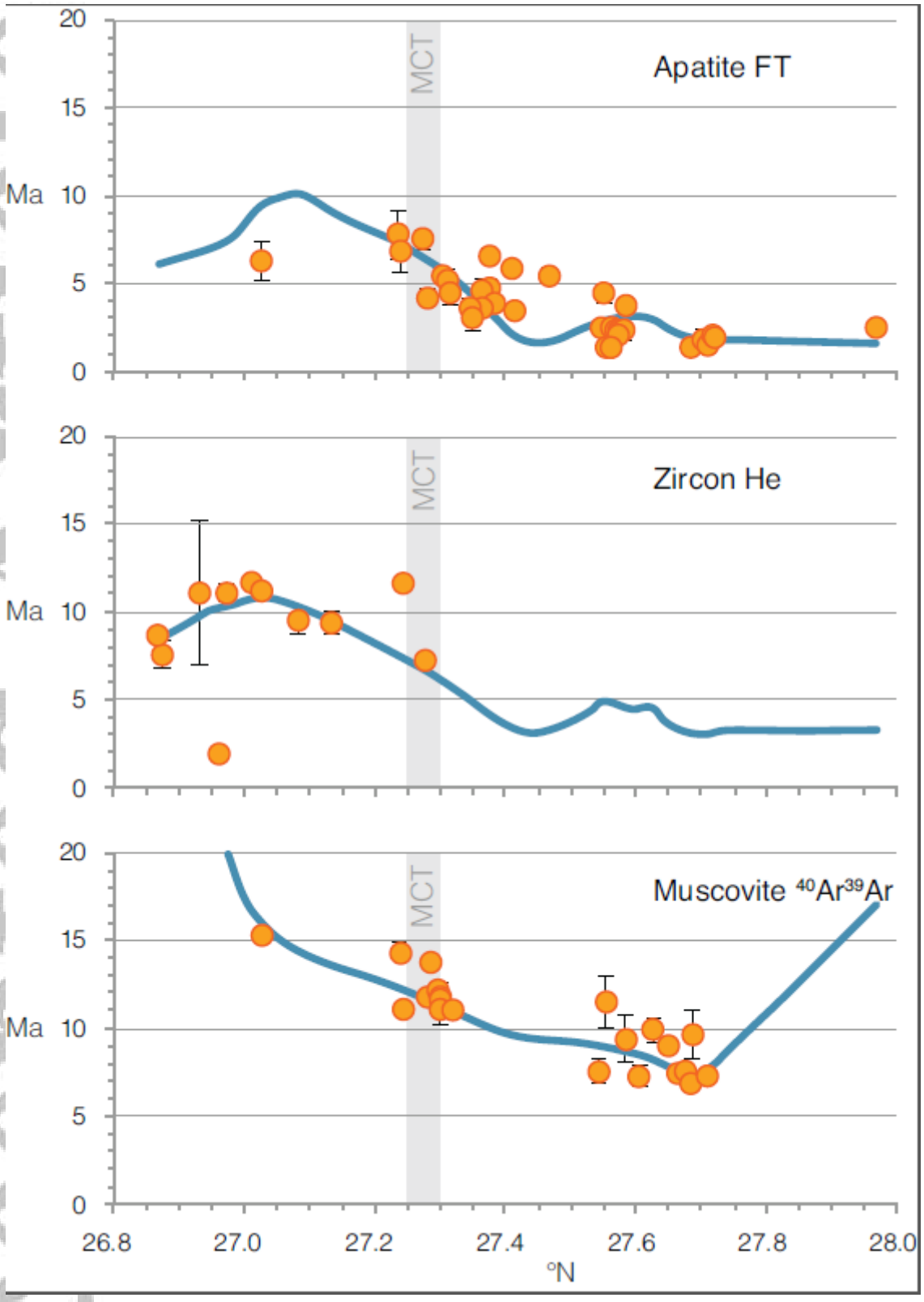


**Figure 10.** Comparison between observed (orange circles) and predicted (blue line, defined by 62 model points) thermochronological ages. (a) apatite U-Th/He ages; (b); apatite fission-track ages (c) zircon U-Th/He ages; (d) muscovite $^{40}Ar/^{39}Ar$ ages.

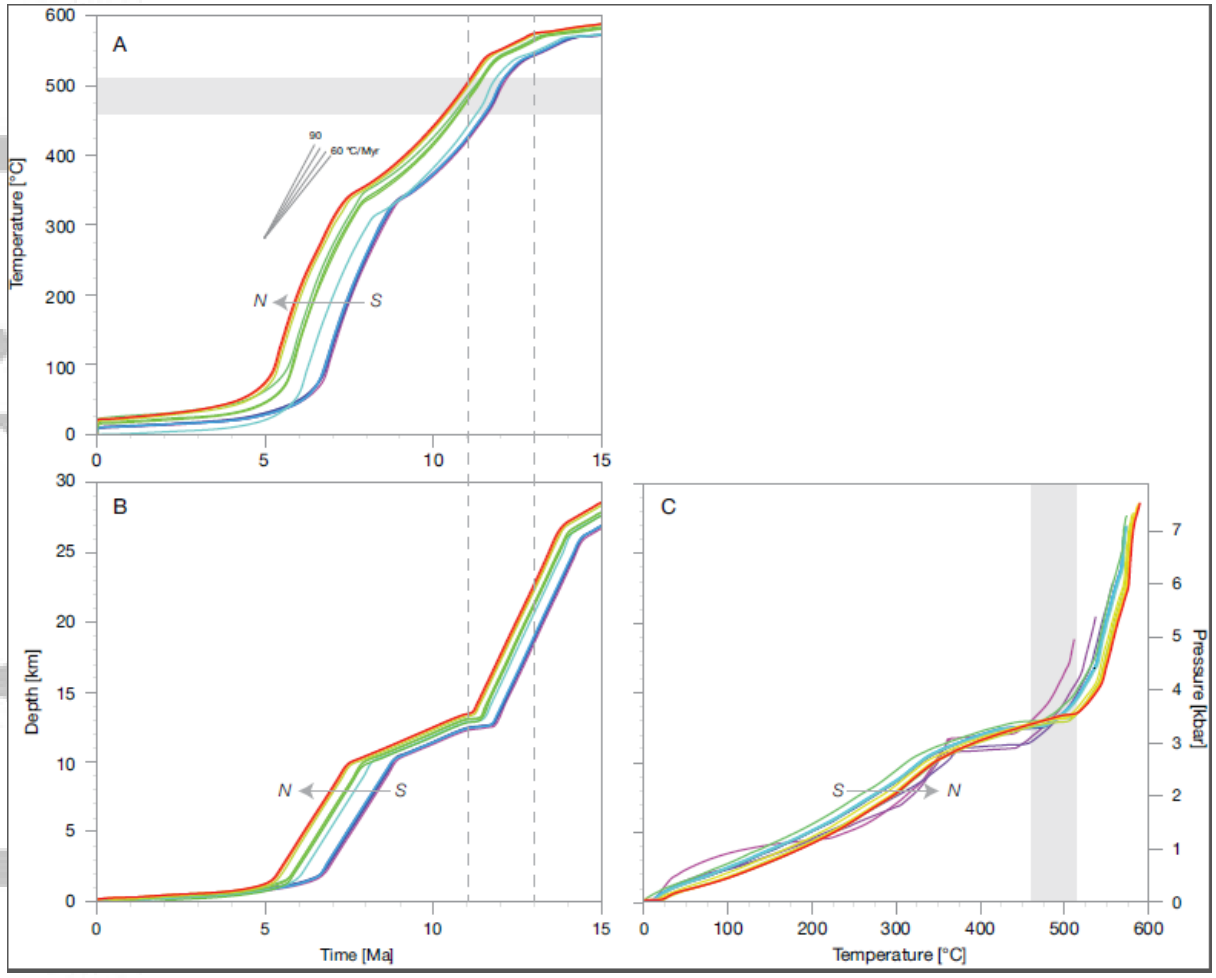


**Figure 11.** Time-temperature-depth paths of model particles in the upper LHS, the base of the MCT shear zone. The paths are arranged from south (purple) to north (red), i.e., structurally from bottom to the top. Gray bars indicate the here calculated closure temperature range for the muscovite $^{40}Ar/^{39}Ar$ dates.

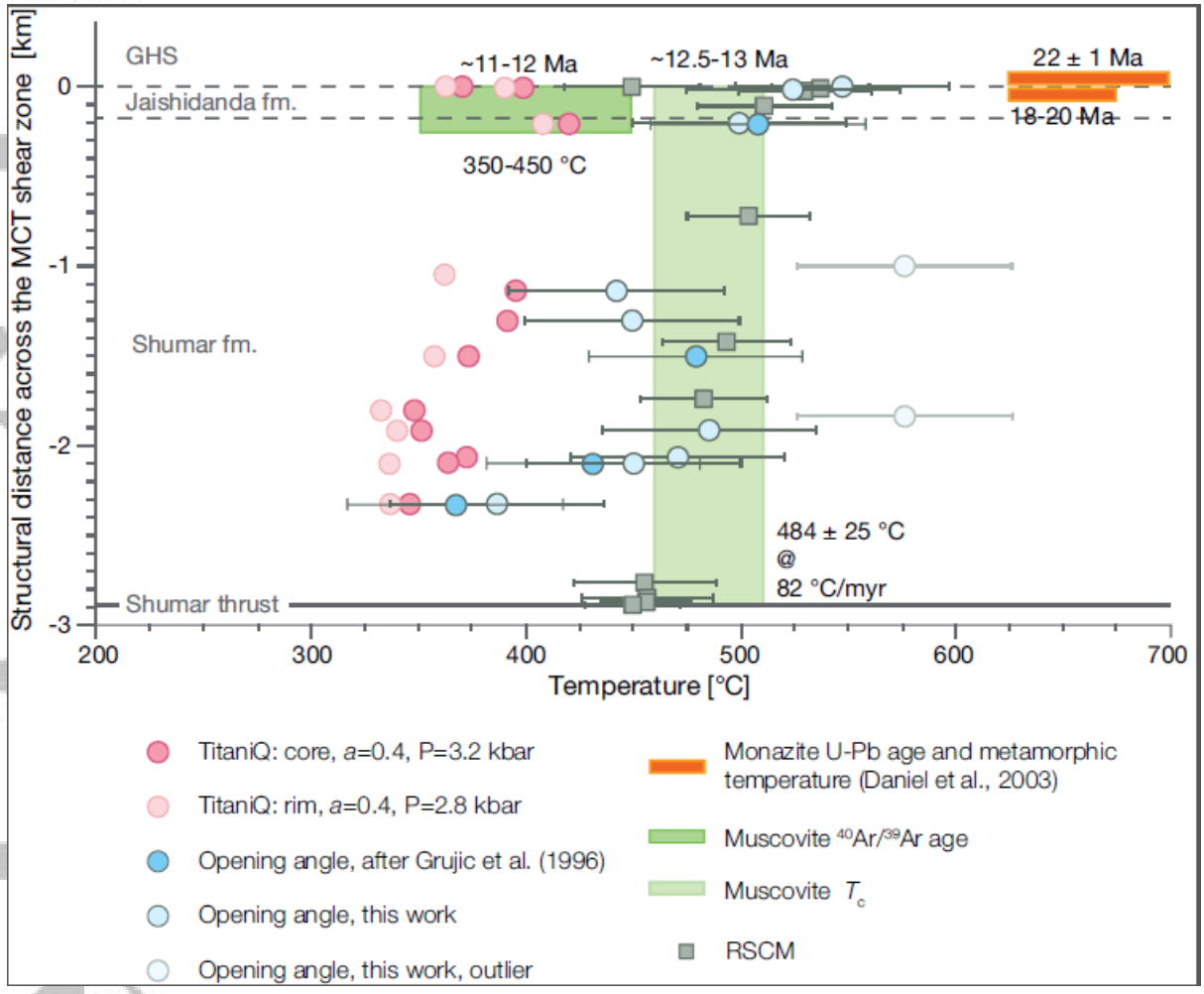


**Figure 12** Deformation temperatures and metamorphic temperatures in the LHS of eastern Bhutan plot with the structural distance from the MCT. Peak Ti-in-quartz temperatures were calculated at 9 kbar according to thermobarometric estimates by Daniel et al. (2003). Peak Ti-in-quartz temperatures for quartz grain cores are the maximum estimates; at lower titania activities the deformation temperatures would have been higher than the RSCM temperatures at the same locations. Deformation temperatures for quartz rims are minimum estimates. The corresponding pressure of 4 kbar is estimated from the published PT paths (Daniel et al., 2003), the titania activity of 0.4 (consistent with a system buffered by Ti-bearing biotite) yields temperatures closest to the metamorphic temperature at 4 kbar. Higher activity would yield temperatures lower than the deformation temperatures estimated from the quartz microstructure and would be minimum estimates. RSCM data are reported with the 2 SEM (Table 1). Deformation temperatures determined by *c*-axis fabric opening-angle thermometry are reported with ± 50 °C calibration error. Symbols in faded colors are outlier temperatures that may explained by the role of water weakening and strain rate in controlling the opening angle (Law, 2014).